Theoretical study of intermolecular proton transfer using diabatic potential

メタデータ	言語: eng 出版者: 公開日: 2018-02-27 キーワード (Ja): キーワード (En): 作成者: メールアドレス: 所属:
URL	http://hdl.handle.net/2297/00050243

This work is licensed under a Creative Commons Attribution-NonCommercial-ShareAlike 3.0 International License.

Doctoral Dissertation

Theoretical study of intermolecular proton transfer using diabatic potential

Division of Material Chemistry,
Graduate School of Natural Science and Technology,
Kanazawa University

Student ID Number: 1424022005

Yuta Hori

Chief supervisor: Tomonori Ida

January, 2017

Contents

Chapter 1

Introduction

One of the important steps in the theoretical treatment of chemical reactions is representation of the potential energy surface (PES) [1, 2]. PES gives not only the local geometries such as reactant (RS), transition (TS), and product states (PS), but the energy landscape for various configurational changes in chemical reactions. Most approaches to chemical reactions analyze the PES by quantum chemical calculations derived under the Born-Oppenheimer approximation, also known as the adiabatic PES. Once the PES is obtained, the scattering cross section, reaction constant, and reaction path, which are important for understanding chemical reactions, can be obtained from the PES [3]. Therefore the PES can be used to elucidate the detail of chemical reactions. Although ab initio quantum chemical calculations are becoming possible for large molecular systems, however, accurate PES calculations for understanding chemical reactions tend to be unfeasible. In addition, though analytical function for PES requires to analyze the

reaction, the global function has not been known.

One of the ways for dealing with the problem has been to use intrinsic reaction coordinate (IRC). IRC is the PES only along a one-dimensional curve that connects RS, TS, and PS, which is the most important reaction path in chemical reactions. Though this approach has been very useful, IRC requires the TS configuration, the computational cost of which makes the calculation difficult for large molecular systems.

Rather than examine the adiabatic PES, another approach to chemical reactions is to analyze the diabatic PES. In contrast to the adiabatic potential, the diabatic potential presents electronic states that change constantly to confine the eigenstates of the electronic Hamiltonian. There are some approaches to describing the diabatic potential [4], constructing using some valence bond (VB) electronic wave functions [5–8]. For empirical valence bond (EVB) [9] or multistate empirical valence bond (MS-EVB) [10] approaches, diabatic potentials are used to provide the molecular mechanical functions needed to construct the PES [11–27]. Therefore, a proposal of simple method for light or more uniquely construction of PES in the diabatic picture is important to analyze the chemical reaction and it can be widely applied to describing large molecular systems such as protains.

Meanwhile, detailed analyses of chemical reactions such as proton transfer require a quantum mechanical treatment. One of the approaches to quantum mechanical treat-

ments is a time-dependent reactive scattering for estimating individual scattering matrix (S-matrix) elements. S-matrix elements have been obtained from time-correlation functions between RS and PS wavepackets. Furthermore, Miller and co-workers [28–30] have used the reactant partition function to show that cumulative reaction probability can be directly related to the thermal rate constant. However, in general the reactive scattering approach intrinsically tends to be complicated and imbalanced because the least and most appropriate wavefunctions corresponding to the RS and PS wavepackets are required in order to calculate the time-correlation functions.

In the diabatic picture, the Hamiltonian is divided into nonreactive (reactant and product) and reactive parts. In particular, the reaction probability based on the reactive scattering theory is evaluated in terms of the transition between two nonreactive surfaces. The wavefunctions corresponding to the RS and PS necessary for calculating the time-correlation functions can be easily obtained in the diabatic picture. Therefore reactive scattering approach in the diabatic picture are important for analyzing proton transfer reactions based on a quantum mechanical treatment.

In this dissertation, a simple construction method of global PES and analytical method using the PES for intermolecular proton transfer are mainly discussed. The content of this dissertation is as follows. Chapter 2 shows the fundamental theories used in this dissertation. Chapter 3 is discussed a construction method of PES in

diabatic picture for intermolecular proton transfer. In this chapter, we focus on the proton-bonded ammonia ($AmH^+ - Am$) and imidazole ($ImH^+ - Im$) pairs as homo-molecular proton transfer systems and the proton-bonded imidazole-ammonia ($ImH^+ - Am$) and ammonia-water ($AmH^+ - Wat$) as hetero-molecular systems. Chapter 4 is discussed a thermal rate constant estimation method for intermolecular proton transfer reactions that uses quantum dynamics simulations on the constructed potentials. In this chapter, we focus on the proton-bonded water ($WatH^+ - Wat$) and $AmH^+ - Am$ pairs as homo-molecular proton transfer systems, and on$AmH^+ - Wat$ pair as hetero-molecular systems. Chapter 5 shows the application to intermolecular proton transfer in proton conductive material using the diabatic picture. In this chapter, the approaches discussed in chapters 3 and 4 are applied to crystalline imidazolium succinate (Im-Suc), which is a known proton-conductive material. Chapter 6 shows the analysis of the reaction involving proton using adiabatic potential instead of diabatic potential. This chapter is discussed the hydride transfer process including a proton during the reduction of formaldehyde by $LiAlH_4$ and $LiBH_4$, including investigations of the geometries, solvent effects and charge transfer processes along the IRC. Finally, chapter 7 shows conclusion of this dissertation entire.

Chapter 2

Fundamental Theory

In this chapter, fundamental theories used in this dissertation are discussed. To analyze chemical reactions by the theoretical treatment, in general quantum chemical calculation is performed. Especially a potential energy surface (PES) using the quantum chemical calculation is usually constructed based on the Born-Oppenheimer approximation. Therefore, "Quantum chemical calculation" and "Born-Oppenheimer approximation" are explained in sections 1 and 2, respectively. Once the PES is obtained, the potential gives the energies and configurations of reactant, transition, and product states as one example. Reaction rate constant of the reaction can be then estimated base on transition state theory using information of reactant and transition states. "Transition state theory" is explained in section 3, which is one of the important theories for estimation of rate constant. A main topic of this dissertation is an analysis of proton transfer using diabatic PES. The Diabatic PES are based on diabatic representation, while adiabatic

PES, which are usually used, are based on adiabatic representation. Therefore, “Adiabatic and Diabatic representation” is explains in section 4. Proton transfer reaction is often included nuclear quantum effect and treated quantum mechanical approaches. In this dissertation, quantum mechanical approach such as quantum wavepacket dynamics is performed. Therefore, “Quantum wavepacket dynamics” is explained in section 5. Finally, “Quantum theory of chemical reaction” is explained section 6.

2.1 Quantum chemical calculation

In this dissertation quantum chemical calculations are performed by using density functional theory (DFT). In this section, the fundamental theory of DFT and basis function for the quantum chemical calculation is discussed. A more detailed description of the DFT and basis function is given in Ref. [31–34]. The outline of them is discussed in the following.

2.1.1 Density functional theory

The basis for DFT was proven by Hohenberg and Kohn [35] that the ground-state electronic energy is determined completely by the electron density. Thus, DFT does not attempt to calculate the wave function with $3N$ coordinates for an N electron molecular system but calculates the electron probability density with three coordinates

and calculates the electronic energy from the density. Therefore, DFT is the method with light computational cost than the post-Hartree-Fock methods such as configuration interaction (CI), Møller-Plesset (MP), and coupled cluster (CC) approaches including electron correlation.

The most common implement of DFT was achieved through the Kohn-Sham (KS) method [36]. Kohn and Sham considered a fictitious system of N non-interacting electrons that have for their overall grand-state density the same density as some real system of interest where the electrons do interact. The formalism of KS method is as follows. First, the energy functional with electron density was divided into specific components to facilitate further analysis, especially:

$$D_{\mathrm{DFT}}[\rho] = T_{\mathrm{S}}[\rho] + V_{\mathrm{ne}}[\rho] + V_{\mathrm{ee}}[\rho] + \Delta T[\rho] + \Delta V_{\mathrm{ee}}[\rho], \tag{2.1}$$

where $T_{\mathrm{S}}[\rho]$ is the kinetic energy term of the non-interacting electrons, $V_{\mathrm{ne}}[\rho]$ is the nuclear-electron interaction term, $V_{\mathrm{ee}}[\rho]$ is the classical electron-electron repulsion term, $\Delta T[\rho]$ is the correction to the kinetic energy deriving from the interacting nature of the electrons, and $\Delta V_{\mathrm{ee}}[\rho]$ is the all non-classical corrections to the electron-electron repulsion tern. For a non-interacting system of electrons, the kinetic energy is just the sum of the individual electron kinetic energies. Within an orbital for the density based

on a Slate determinant wave function, Eq. (2.1) may be then rewritten as

$$D_{\mathrm{DFT}}[\rho] = \sum_{i}^{N} \left(\langle \phi_i | - \frac{1}{2}\nabla_i^2 | \phi_i \rangle - \langle \phi_i | \sum_{k}^{\text{nuclei}} \frac{Z_k}{|r_i - r_k|} | \phi_i \rangle \right) + \sum_{i}^{N} \langle \phi_i | \frac{1}{2} \int \frac{\rho(r')}{|r_i - r'|} dr' | \phi_i \rangle + E_{\mathrm{xc}}[\rho], \tag{2.2}$$

where N is the number of electrons and a Slater determinant wave function is used satisfying simply

$$\rho = \sum_{i}^{N} \langle \phi_i | \phi_i \rangle. \tag{2.3}$$

$E_{\mathrm{xc}}[\rho]$ is $\Delta T[\rho] + \Delta V_{\mathrm{ee}}[\rho]$ in Eq. (2.1), which is referred to as the exchange-correlation energy. By minimizing $D_{\mathrm{DFT}}[\rho]$ in Eq. (2.2) with respect to variation of the orbitals $\{\phi_i\}$, it is then derived the following KS equation:

$$h_i^{\mathrm{KS}} \phi_i = \varepsilon_i \phi_i, \tag{2.4}$$

where the KS one-electron operator is defined as

$$h_i^{\mathrm{KS}} = -\frac{1}{2}\nabla_i^2 - \sum_{k}^{\text{nuclei}} \frac{Z_k}{|r_i - r_k|} + \int \frac{\rho(r')}{|r_i - r'|} dr' + V_{\mathrm{xc}}, \tag{2.5}$$

and

$$V_{\mathrm{xc}} = \frac{\delta E_{\mathrm{xc}}}{\delta \rho}. \tag{2.6}$$

A set of canonical KS orbitals $\{\phi_i\}$ in Eq. (2.4) is determined by numerical methods or expansion in a set of basis functions. Insofar as the density is required for computation of the KS operator, but the density is determined using the orbitals derived from solution of KS equation, the KS process thus must be carried out as an iterative SCF procedure. If the exact $E_{\mathrm{xc}}[\rho]$ was known, DFT would provide the exact total energy including electron correlation. Although it is possible to prove that the exchange-correlation potential is a unique functional for all systems, however, an explicit functional form of this potential has been elusive. The difference between DFT methods is the choice of the functional form of the exchange-correlation energy E_{xc}.

It is customary to separate E_{xc} into two parts: a pure exchange E_{x} and a correlation part E_{c}, although it is not clear that this is a valid assumption. Each of these energies is often written in terms of the energy density, ε_{x} and ε_{c}:

$$E_{\mathrm{xc}}[\rho] = E_{\mathrm{x}}[\rho] + E_{\mathrm{c}}[\rho] = \int \rho(r)\varepsilon_{\mathrm{x}}[\rho(r)]dr + \int \rho(r)\varepsilon_{\mathrm{c}}[\rho(r)]dr. \tag{2.7}$$

In the Local Density Approximation (LDA) it is assumed that the density locally can be treated as a uniform electron gas, or equivalently that the density is a slowly varying

function. The exchange energy for a uniform electron gas is then given by the Dirac formula [37]:

$$E_{\mathrm{x}}^{\mathrm{LDA}}[\rho] = -C_{\mathrm{x}} \int \rho^{4/3}(r) dr, \tag{2.8}$$

$$\varepsilon_{\mathrm{x}}^{\mathrm{LDA}}[\rho] = -C_{\mathrm{x}} \rho^{1/3}. \tag{2.9}$$

In general the LDA underestimates the exchange energy by $\sim 10\%$, thereby creating errors which are larger than the whole correlation energy. Electron correlation is furthermore overestimated and bond strengths are as a consequence overestimated. The most fundamental process in chemistry is the making and breaking of bonds. Computation of bond energies is therefore one of the greatest concerns of quantum chemists. Therefore an obvious way to improve on LDA is to allow the exchange correlation energy per particle to depend not only on the density at the point r, but also on the density gradients ($\nabla\rho$). This generalizes Eq. (2.7) to the form:

$$E_{\mathrm{xc}}^{\mathrm{GGA}}[\rho] = \int f(\rho(r), \nabla\rho) dr, \tag{2.10}$$

where the function f is chosen by some set of criteria. Such approximation is called generalized gradient approximation (GGA), and variety of different forms for function f have been suggested and applied in the literature. One of the most commonly

used exchange functionals is B88 proposed by Becke [38], which was corrected to $-r^{-1}$ asymptotic behavior for the energy density:

$$\varepsilon_{\rm x}^{\rm B88} = \varepsilon_{\rm x}^{\rm LDA} + \Delta\varepsilon_{\rm x}^{\rm B88}, \tag{2.11}$$

$$\Delta\varepsilon_{\rm x}^{\rm B88} = -\beta\rho^{1/3}\frac{x^2}{1+6\beta x\sinh^{-1}x},$$

where β is the parameter determined by fitting to known atomic data and $x = |\nabla\rho|/\rho^{4/3}$. Also, one popular gradient corrected functional for correlation energy is due to Lee, Yang, and Parr (LYP) [39], and has the form:

$$\begin{aligned}
\varepsilon_c^{\rm LYP} =& -a\frac{\gamma}{(1+d\rho^{-1/3})} - ab\frac{\gamma e^{-c\rho^{-1/3}}}{9(1+d\rho^{-1/3})\rho^{8/3}} \\
&\times\left[\begin{array}{l} 18(2^{2/3})C_F(\rho_\alpha^{8/3}+\rho_\beta^{8/3}) - 18\rho t_W \\ \\ +\rho_\alpha(2t_W^\alpha+\nabla^2\rho_\alpha)+\rho_\beta(2t_W^\beta+\nabla^2\rho_\beta)\end{array}\right], \\
\gamma =& \ 2\left[1-\frac{\rho_\alpha^2+\rho_\beta^2}{\rho^2}\right], \\
t_W^\sigma =& \ \frac{1}{8}\left(\frac{|\nabla\rho_\sigma|^2}{\rho_\sigma}-\nabla^2\rho_\sigma\right), \\
C_F =& \ \frac{3}{10}(3\pi^2)^{2/3},
\end{aligned} \tag{2.12}$$

where the parameters a, b, c and d are determined by fitting to data for the helium atom. The t_W functional is known as the local Weizsacker kinetic energy density.

Prior to a more detailed analysis of performance, at least in functional design, the inclusion of Hartree-Fock (HF) exchange is considered. The Slater determinant of KS orbitals is the exact wave function for the non-interacting Hamiltonian operator. Therefore, the expectation value is the exact exchange for the non-interacting system, which can be computed just as it is in HF calculations except that the KS orbitals are used. Hybrid functionals are a class of approximation to the exchange-correlation energy functional in DFT that incorporate a portion of exact exchange from HF theory.

The exchange-correlation energy functional E_{XC} is then expressed by using some choice of DFT functional $E_{\mathrm{XC}}^{\mathrm{DFT}}$ as

$$E_{\mathrm{xc}} = (1-a)E_{\mathrm{xc}}^{\mathrm{DFT}} + aE_{\mathrm{x}}^{\mathrm{HF}}, \tag{2.13}$$

where $E_{\mathrm{x}}^{\mathrm{HF}}$ is the exchange functional by using HF theory. One of the most commonly used models in computational chemistry is B3LYP [40], which is defined by

$$E_{\mathrm{xc}}^{\mathrm{B3LYP}} = (1-a)E_{\mathrm{x}}^{\mathrm{LSDA}} + aE_{\mathrm{x}}^{\mathrm{HF}} + b\Delta E_{\mathrm{x}}^{\mathrm{B}} + (1-c)E_{\mathrm{c}}^{\mathrm{LSDA}} + cE_{\mathrm{c}}^{\mathrm{LYP}}, \tag{2.14}$$

where a, b, and c were optimized to 0.20, 0.72, and 0.81, respectively. The name of the functional, B3LYP, implies its use of a three-parameter scheme, as well as the GGA exchange and correlation functions Becke and Lee-Yang-Parr, respectively.

Hybrid functionals are a slight improvement, but not nearly enough. Long range corrected (LC) methods have been proposed that divide the interelectronic interaction $1/r_{12}$ into a short-range part and a long-range part:

$$\frac{1}{r_{12}} = \frac{1 - \mathrm{erf}(\omega r_{12})}{r_{12}} + \frac{\mathrm{erf}(\omega r_{12})}{r_{12}}. \tag{2.15}$$

The first term accounts for the short range interaction, and the second term accounts for the long range interaction. CAM-B3LYP is a long-range corrected version of B3LYP that employs the Coulomb-attenuating method [41]. Although the conventional B3LYP method is typically used to investigate charge density [42] and solvent effects [43], CAM-B3LYP improves upon B3LYP since the latter is unsuccessful in a number of important applications, such as when determining the polarizability of long chains, excitations of Rydberg states and especially charge transfer effects [44–46]. In this thesis, the quantum chemical calculations were carried out using B3LYP and CAM-B3LYP functionals.

2.1.2 Basis function

The basis functions are the mathematical functions to construct wave functions. The electron density is expressed as a Slater determinant formed from the set of canonical KS orbitals $\{\phi_n\}$ in KS-DFT theory. Each orbital is expressed as a linear combination

of basis functions, the coefficients for which are determined from the iterative SCF procedure.

There are two type of basis functions commonly used in quantum chemical calculations: Slater Type Orbitals (STO) and Gaussian Type Orbitals (GTO). STO and GTO have the functional forms, respectively:

$$\chi^{\mathrm{STO}}_{\xi,n,l,m}(r,\theta,\phi) = NY_{l,m}(\theta,\phi)r^{n-1}e^{-\xi r}, \tag{2.16}$$

$$\chi^{\mathrm{GTO}}_{\xi,l_x,l_y,l_z}(x,y,z) = Nx^{l_x}y^{l_y}z^{l_z}e^{-\xi r^2}, \tag{2.17}$$

where N is normalization constant, $Y_{l,m}$ is the usual spherical harmonic functions, and the sum of l_x, l_y, and l_z determines the type of orbital. Although the exponential dependence of STO on the distance between the nucleus and the electron describes the exact orbitals for the hydrogen atom, however, the calculation using the STO is computationally effort because of not having analytical three- and four- center two-electron integrals. On the other hand, the calculation using the GTO is computationally efficient because of having analytical solution of the general two-electron integral. However, the r^2 dependence in the exponential makes the GTO inferior to the STO in two aspects. At the nucleus the GTO has zero slope, in contrast to the STO which has " cusp " and GTO has problems representing the proper behavior nucleus. The other problem

is that the GTO falls off too rapidly far from the nucleus compared with an STO, and the “ tail ” of the wave function is consequently represented poorly.

Both STO and GTO can be chosen to form a complete basis, but the above considerations indicate that more GTOs are necessary for achieving a certain accuracy compared with STOs. A rough guideline says that the basis functions used for SCF calculations were not individual GTOs, but instead a linear combination of GTOs fit to reproduce as accurately as possible as STO, then it is referred to as a “contracted” GTO (CGTO), and the individual Gaussian form, which is called “ primitive ” Gaussians, i.e.,

$$\chi(\text{CGTO}) = \sum_{i}^{k} a_i \chi_i(\text{PGTO}). \tag{2.18}$$

where χ_i's are normalized Gaussians. The contraction coefficients a_i are constants that are held fixed during the calculation. By using contracted Gaussians instead of primitive Gaussians as the basis set, the number of variational coefficients to be determined is reduced, which gives large savings in computational time with little loss in accuracy if the contraction coefficients a_i are well chosen. In terms of computational efficiency, CGTOs are therefore preferred, and used almost universally as basis functions in quantum chemical calculations.

Correlation consistent basis function

The correlation consistent (cc) basis functions are geared toward recovering the correlation energy of the valence electrons, thus the exponents and contraction coefficients are variationally optimized not only for HF calculations, but also for calculations including electron correlation (such as CI). They are designed to converge systematically to the complete-basis-set (CBS) limit using empirical extrapolation techniques. There are known by their acronyms: cc-pVDZ, cc-pVTZ, cc-pVQZ, cc-pV5Z, cc-pV6Z. Note that as we go from one basis set to the next, the number of sets of basis functions of each angular-momentum l value is increased by one and one set of functions with the next higher l value is added. The addition of diffuse primitive nonpolarization and polarization functions to the cc-pVnZ basis sets gives the augmented sets aug-cc-pVDZ, aug-cc-pVTZ, etc., suitable for calculations on anions and hydrogen bonded species. To form the set aug-cc-pVnZ from cc-pVnZ, the number of sets of basis functions of each angular-momentum l value is increased by one by the addition of diffuse primitives.

In this dissertation, when quantum chemical calculation were performed, aug-cc-pVDZ and aug-cc-pVTZ as the basis sets were used.

2.2 Born-Oppenheimer approximation

A potential energy surface (PES) using the quantum chemical calculation is usually constructed based on the Born-Oppenheimer (BO) approximation. BO approximation is also central to quantum chemistry. In this section, the outline is explained.

For a general molecular system consisting of electrons and nuclei, the Hamiltonian can be written as

$$H(r, R) = T_N + T_e(r) + V_{eN}(r, R) + V_{ee}(r, R) + V_{NN}, \tag{2.19}$$

where T_N represents the nuclear kinetic energy operator; T_e represents the electronic kinetic energy operator; V_{eN} is electron-nuclear interaction; V_{ee} is electron-electron interaction; and V_{NN} is nuclear-nuclear interaction. We use r and R as collective indices to denote the coordinates of the electrons and nuclei, respectively. Since nuclei are much heavier than electrons, they move more slowly. Hence, to a good approximation, one can consider the electrons in a molecule to be moving in the field of fixed nuclei. Within this approximation, T_N can be neglected and V_{NN} can be considered to be constant. The remaining terms in Eq. (2.19) are called the electronic Hamiltonian:

$$H_{el} = T_e(r) + V_{eN}(r, R) + V_{ee}(r, R). \tag{2.20}$$

We then obtain the Schrödinger equation involving electronic Hamiltonian:

$$H_{el}\phi_n^{el}(r;R) = E_{el}\phi_n^{el}(r;R). \tag{2.21}$$

The electronic wave function ϕ_n^{el} describes the motion of the electrons and explicitly depends on the electronic coordinates but depends parametrically on the nuclear coordinates. The total energy for fixed nuclei include the constant nuclear repulsion:

$$E_{tot} = E_{el} + V_{NN}. \tag{2.22}$$

Within BO approximation, a nuclear Hamiltonian can be described as the motion of the nuclei in the average field of the electrons,

$$H_{nucl} = T_N + E_{tot}. \tag{2.23}$$

Therefore the total energy E_{tot} provides a potential for nuclear motion and the function constitutes a PES. Thus the nuclei in the BO approximation move on a PES obtained by solving the electronic problem or performing quantum chemical calculations.

2.3 Transition state theory

Transition state theory (TST) explains the reaction rates of elementary chemical reactions, which was developed by Henry Eyring [47], Meredith Gwynne Evans and Michael Polanyi [48]. TST, which assumes a quasi-equilibrium between reactant (RS) and activated transition state (TS), provides a simple way of formulating reaction rates and gives a unique insight into how processes occur. The theory is conveniently classified under three headings: (1) thermodynamic treatments, (2) kinetic-theory treatments, and (3) statistical-mechanical treatments. In addition, TST is based on these three postulates:

1. In passing from RS to product state (PS) over the potential energy surface, the reacting system must traverse a region of the reaction path called the TS. The rates of reaction can be estimated by examining only TS.

2. The chemical species in the TS is in quasi-equilibrium with the RS.

3. The rate of reaction is equal to the product of the concentration of TS species formed from the RS and the frequency with which this species passes on the PS.

The rate constant based on the TST is derived as follow.

We consider the bimolecular reaction of A with B to form P, but in which A and B reversibly react to form an intermediate complex $[AB]^{\ddagger}$, which irreversibly decomposes

to form final product P, i.e.,

$$A + B \rightleftharpoons [AB]^{\ddagger} \rightarrow P. \tag{2.24}$$

TST assumes that the activated complexes are in quasi-equilibrium with the reactants. The equilibrium constant $K^{\ddagger}$ for the quasi-equilibrium can be written as

$$K^{\ddagger} = \frac{[AB]^{\ddagger}}{[A][B]}. \tag{2.25}$$

The concentration of the TS $[AB]^{\ddagger}$ is then given by

$$[AB]^{\ddagger} = K^{\ddagger}[A][B] \tag{2.26}$$

Therefore, the rate equation for the production of PS is written as

$$\frac{d[P]}{dt} = k^{\ddagger}[AB]^{\ddagger} = k^{\ddagger}K^{\ddagger}[A][B] = k[A][B], \tag{2.27}$$

where the rate constant k is given by

$$k = k^{\ddagger}K^{\ddagger}. \tag{2.28}$$

$K^{\ddagger}$ is expressed in terms of the partition functions for the activated complex, therefore k is given by

$$k = k^{\ddagger} \frac{Q^{\ddagger'}}{Q_A Q_B} e^{-\Delta E_0^{\ddagger}/k_B T}, \tag{2.29}$$

where

$$\Delta E_0^{\ddagger} = E^{\ddagger} - E_0. \tag{2.30}$$

Q_A, Q_B, and $Q^{\ddagger'}$ contains terms for translational motion, rotation around the center of mass, and electronic energy for A, B, and $AB^{\ddagger}$, respectively. Although we assume that partition functions in RS and TS, the TS has one less degree of vibrational freedom than the RS. Therefore, instead of $3N-6$ degrees of vibrational freedom, it has $3N-7$ degrees of vibrational freedom for TS. The vibration can be then expressed along the reaction coordinate (r.c.) as a one-dimensional translational partition function $Q_{\text{r.c.}}$:

$$Q_{\text{r.c.}} = \left(\frac{2\pi m^{\ddagger} k_B T}{h^2} \right)^{\frac{1}{2}} \delta, \tag{2.31}$$

where $m^{\ddagger}$ is the mass of the molecule in which the bond is breaking and δ is the width of the barrier across the saddle point of the TS. The term on the right hand side of Eq.

(2.29) is factored out of the partition function $Q^{\ddagger}$:

$$k = k^{\ddagger} \left(\frac{2m^{\ddagger} k_B T}{h^2} \right)^{\frac{1}{2}} \delta \frac{Q^{\ddagger}}{Q_A Q_B} \exp\left(\frac{-\Delta E_0^{\ddagger}}{k_B T} \right). \tag{2.32}$$

We consider the motion only from left to right. The velocity across the top of the barrier is $1/2m^{\ddagger}v^2$. In addition, considering the Boltzmann distribution, we can write down the ratio to the molecules in the TS with velocity v and to the molecules in the TS with velocity zero:

$$\bar{v} = \frac{\int_0^{\infty} v \exp\left(\frac{-1/2mv^2}{k_B T} \right) dv}{\int_0^{\infty} \exp\left(\frac{-1/2mv^2}{k_B T} \right) dv} = \left(\frac{k_B T}{2\pi m^{\ddagger}} \right)^{1/2}. \tag{2.33}$$

The rate equals velocity divided by distance, which is given by

$$k^{\ddagger} = \frac{\bar{v}}{\delta}. \tag{2.34}$$

The rate of passage across the barrier is then given by the following equation:

$$k^{\ddagger} = \frac{1}{\delta} \left(\frac{k_B T}{2\pi m^{\ddagger}} \right)^{1/2}. \tag{2.35}$$

This means that k is given by the following expression:

$$k = \frac{1}{\delta}\left(\frac{k_B T}{2\pi m^{\ddagger}}\right)^{1/2}\left(\frac{2\pi m^{\ddagger} k_B T}{h^2}\right)^{1/2}\delta\frac{Q^{\ddagger}}{Q_A Q_B}\exp\left(\frac{-\Delta E_0^{\ddagger}}{k_B T}\right). \tag{2.36}$$

The absolute rate constant $k^{\ddagger}$ is finally written as

$$k^{\ddagger} = \frac{k_B T}{h}, \tag{2.37}$$

and k is

$$k = \frac{k_B T}{h}\frac{Q^{\ddagger}}{Q_A Q_B}\exp\left(-\frac{\Delta E_0^{\ddagger}}{k_B T}\right). \tag{2.38}$$

Additionally, by analogy with the thermodynamic relation $\Delta G = \Delta H - T\Delta S, K^{\ddagger}$ can be written as

$$K^{\ddagger} = e^{-\Delta G^{\ddagger}/RT}. \tag{2.39}$$

Therefore, Eq. (2.38) gives the following Eyring equation:

$$k = \frac{k_B T}{h}\exp\left(-\frac{\Delta G_0^{\ddagger}}{RT}\right) = \frac{k_B T}{h}\exp\left(\frac{\Delta S_0^{\ddagger}}{R}\right)\exp\left(-\frac{\Delta H_0^{\ddagger}}{RT}\right). \tag{2.40}$$

TST usually describes well low dimensional systems such as chemical reactions in the gas phase. Even though the theory is widely applicable, however, it does have limitations.

For example, when applied to each elementary step of a multi-step reaction, the theory assumes that each intermediate is long-lived enough to reach a Boltzmann distribution of energies before continuing to the next step. When the intermediates are very short-lived, however, then TST fails. TST is also based on the assumption that atomic nuclei behave according to classic mechanics. It is assumed that unless atoms or molecules collide with enough energy to form the transition structure, then the reaction does not occur. However, according to quantum mechanics, for any barrier with a finite amount of energy, there is a possibility that particles can still tunnel across the barrier. With respect to chemical reactions this means that there is a chance that molecules will react even if they do not collide with enough energy to traverse the energy barrier. While this effect is expected to be negligible for reactions with large activation energies, it becomes a more important phenomenon for reactions with relatively low energy barriers, since the tunneling probability increases with decreasing barrier height. While TST fails for some reactions not only at low temperature but also high temperature. The theory assumes the reaction system will pass over the lowest energy saddle point on the potential energy surface. While this description is consistent for reactions occurring at relatively low temperatures, at high temperatures, molecules populate higher energy vibrational modes; their motion becomes more complex and collisions may lead to transition states far away from the lowest energy saddle point.

2.4 Adiabatic and Diabatic representations

In this dissertation, potential energy surface (PES) for intermolecular proton transfer was constructed. PES is constructed by using adiabatic or diabatic representations. In this section the conventional formalism of the adiabatic and diabatic representations. Since a more detailed description of these representations is given in Ref. [49], the outline of these formalisms is discussed in this section.

For a general molecular system consisting of electrons and nuclei, the Hamiltonian can be written as

$$H(r, R) = T_N + H_e(r) + V_{eN}(r, R), \tag{2.41}$$

where T_N represents the nuclear kinetic energy operator, H_e is the Hamiltonian of electrons only. V_{eN} includes all the electron-nuclear and nuclear-nuclear interactions. We use r and R as collective indices to denote the coordinates of the electrons and nuclei, respectively.

Adiabatic representation

In the adiabatic representation, the molecular wavefunction $\Psi(r, R)$ can be expanded on adiabatic basis $\phi_n(r, R)$:

$$\Psi(r, R) = \sum_n \chi_n^{\mathrm{ad}}(R)\phi_n(r, R), \tag{2.42}$$

where $\chi_n^{\mathrm{ad}}(R)$ is the corresponding nuclear wavefunction in this representation, and $\phi_n(r, R)$ determines the electronic wavefunction calculated for any value of R as a parameter by the Schrödinger equation:

$$[H_e(r) + V_{eN}(r, R)]\phi_n(r, R) = \epsilon_n(R)\phi_n(r, R). \tag{2.43}$$

The molecular wavefunction $\Psi(r, R)$ then satisfies the time-dependent Schrödinger equation:

$$i\hbar\frac{\partial\Psi(r, R)}{\partial t} = H(r, R)\Psi(r, R). \tag{2.44}$$

Multiplying from the left by $\langle\phi_m|$ in above equation, it gives the following equation:

$$i\hbar\frac{\partial\chi_m^{\mathrm{ad}}(R)}{\partial t} = [T(R) + \epsilon_m(R)]\chi_m^{\mathrm{ad}}(R) + \sum_n \Lambda_{mn}(R)\chi_n^{\mathrm{ad}}(R). \tag{2.45}$$

$\Lambda_{mn}(R)$ is the non-adiabatic coupling matrix operator in the adiabatic representation, which is given by

$$\Lambda_{mn}(R) = -\frac{\hbar^2}{M}\left(\langle\phi_m|\nabla_R|\phi_n\rangle\nabla_R + \frac{1}{2}\langle\phi_m|\nabla_R^2|\phi_n\rangle\right). \tag{2.46}$$

Equation (2.45) can be written in matrix form:

$$i\hbar\frac{\partial\boldsymbol{\chi}^{\mathrm{ad}}(R)}{\partial t} = (\boldsymbol{T} + \boldsymbol{V}^{\mathrm{ad}})\boldsymbol{\chi}^{\mathrm{ad}}(R), \tag{2.47}$$

where the diagonal matrix $\boldsymbol{V}^{\mathrm{ad}}$ is adiabatic potential with diagonal parts of $\epsilon_m(R)$. The nuclear potential operator in the Schrödinger equation is diagonal, while the kinetic energy operator $\boldsymbol{T}$ is included in the non-adiabatic coupling matrix, and is thus not diagonal. For a two-state system, Eq. (2.47) can be expressed in matrix form:

$$i\hbar\frac{\partial}{\partial t}\begin{pmatrix}\chi_1^{\mathrm{ad}}\\ \\ \chi_2^{\mathrm{ad}}\end{pmatrix} = \begin{pmatrix}T_1 & \Lambda_{12}\\ \\ \Lambda_{21} & T_2\end{pmatrix}\begin{pmatrix}\chi_1^{\mathrm{ad}}\\ \\ \chi_2^{\mathrm{ad}}\end{pmatrix} + \begin{pmatrix}\epsilon_1 & 0\\ \\ 0 & \epsilon_2\end{pmatrix}\begin{pmatrix}\chi_1^{\mathrm{ad}}\\ \\ \chi_2^{\mathrm{ad}}\end{pmatrix}. \tag{2.48}$$

In the adiabatic representation, the PES can be obtained by quantum chemical calculations for a given nuclear geometry. Nuclear dynamics problems must be solved using this potential with off-diagonal kinetic energy operators for the nuclei.

Diabatic representation

In the diabatic representation, $\phi_n(r, R_0)$ is used as basis set, the molecular wavefunction $\Psi(r, R)$ can be expanded as

$$\Psi(r, R) = \sum_n \chi_n^{\mathrm{di}}(R)\phi_n(r, R_0). \tag{2.49}$$

$\phi_n(r, R_0)$ is an electronic wavefunction for a fixed reference nuclear configuration R_0, which is selected at a fixed reference value, regardless of the actual spatial positions of the nuclei. $\phi_n(r, R_0)$ determines the electronic wavefunction calculated for a fixed reference nuclear configuration R_0 by the Schrödinger equation:

$$[H_e(r) + V_{eN}(r, R_0)]\phi_n(r, R_0) = \epsilon_n(R_0)\phi_n(r, R_0). \tag{2.50}$$

After multiplying from the left by $\langle\phi_m|$ in Eq. (2.44), the following equation in the diabatic representation is obtained:

$$i\hbar\frac{\partial\chi_m^{\mathrm{di}}(R)}{\partial t} = T_N\chi_m^{\mathrm{di}}(R) + \sum_n V_{mn}^{\mathrm{di}}(R)\chi_n^{\mathrm{di}}(R). \tag{2.51}$$

The off-diagonal elements V_{mn}^{di} arises from the electron-nuclear interaction $V_{eN}(r, R)$ and is given by

$$V_{mn}^{\rm di}(R) = \langle\phi_m|H_e + V_{eN}(R)|\phi_n\rangle = \epsilon_m(R_0)\delta_{mn} + \langle\phi_m|V_{eN}(R) - V_{eN}(R_0)|\phi_n\rangle \quad (2.52)$$

$$= \epsilon_m(R_0)\delta_{mn} + \int \phi_m^*(r, R_0)[V_{eN}(R) - V_{eN}(R_0)]\phi_n(r, R_0)dr.$$

Equation (2.51) can be written in matrix form as

$$i\hbar\frac{\boldsymbol{\chi}^{\rm di}(R)}{\partial t} = (\boldsymbol{T} + \boldsymbol{V}^{\rm di})\chi^{\rm di}(R), \quad (2.53)$$

where the kinetic energy operator $\boldsymbol{T}$ is diagonal, but the potential energy operator $\boldsymbol{V}^{\rm di}$ is off-diagonal with its matrix element given by Eq. (2.52). The diagonal and non-diagonal elements of $\boldsymbol{V}^{\rm di}$ correspond respectively to the diabatic potential and non-adiabatic coupling element in the diabatic representation. For a two-state system, Eq. (2.53) can be expressed in matrix form:

$$i\hbar\frac{\partial}{\partial t}\begin{pmatrix}\chi_1^{\rm di}\\ \\ \chi_2^{\rm di}\end{pmatrix} = \begin{pmatrix}T_1 & 0\\ \\ 0 & T_2\end{pmatrix}\begin{pmatrix}\chi_1^{\rm di}\\ \\ \chi_2^{\rm di}\end{pmatrix} + \begin{pmatrix}V_{11}^{\rm di} & V_{12}^{\rm di}\\ \\ V_{21}^{\rm di} & V_{22}^{\rm di}\end{pmatrix}\begin{pmatrix}\chi_1^{\rm di}\\ \\ \chi_2^{\rm di}\end{pmatrix}, \quad (2.54)$$

where $V_{11}^{\rm di}$ and $V_{22}^{\rm di}$ are diabatic potentials, and $V_{12}^{\rm di}$ and $V_{21}^{\rm di}$ are non-diagonal matrix elements in the diabatic representation.

Relationship between representations

The adiabatic and diabatic representations are related to each other through a unitary transformation. In the subspace of some electronic states, the transformation relation between the representations of nuclear wavefunctions can be obtained as

$$\chi^{\mathrm{ad}} = U\chi^{\mathrm{di}} \tag{2.55}$$

using the diabatic-to-adiabatic transformation matrix U, which is constructed from the electronic wavefunctions sets, where the transformation matrix is given by

$$U_{mn}(R|R_0) = \langle \phi_m(R)|\phi_n(R_0)\rangle = \int \phi_m^*(r,R)\phi_n(r,R_0)dr. \tag{2.56}$$

However, calculation of the transformation matrix U_{mn} is too difficult because it requires the adiabatic and diabatic eigenfucntion sets $\{\phi_m(r,R)\}, \{\phi_n(r,R_0)\}$ for all dimension of r and R, R_0. To avoid this computationally hard condition, we begin with the diabatic representation of Eq. (2.53) by constructing the diabatic coupling potential matrix $\boldsymbol{V}^{\mathrm{di}}$, which is also much easier to calculate than the adiabatic coupling terms.

The adiabatic potential energy matrix V^{ad} is obtained from the diabatic potential

energy matrix V^{di} via

$$V^{\mathrm{ad}} = UV^{\mathrm{di}}U^{\ddagger}. \tag{2.57}$$

For a two-state case, the lowest adiabatic potential energy is then given by the diagonalization of the diabatic potential energy matrix; specifically

$$V^{\mathrm{ad}} = \frac{V_{11}^{\mathrm{di}} + V_{22}^{\mathrm{di}}}{2} - \sqrt{\left(\frac{V_{11}^{\mathrm{di}} - V_{22}^{\mathrm{di}}}{2}\right)^2 + V_{12}^{\mathrm{di}2}}. \tag{2.58}$$

2.5 Quantum wavepacket dynamics

In the quantum mechanical studies, the time-dependent (TD) approach for solving the TD Schrödinger equation has become an extremely important analytical tool for understanding the chemical reactions in the field of theoretical and computational chemistry. TD methods provide clear and direct physical insight into the dynamics in the same way as classical mechanics. The successful development and application of various computational methods for solving the TD Schrödinger equation in the past decade has significantly improved the numerical efficiency for practical applications of the TD methods to chemical dynamics problems with quantum effects.

Especially, quantum wavepacket method is attractive in the problems, because it can visualize the dynamics of the quantum system via a motion of wavepacket, and one

can easily obtain a lot of dynamical information from the results using semiclassical ideas.

In the quantum wavepacket approach a time-step is chosen but the propagation involves updating wavefunction amplitudes at chosen discrete grid points. The wavepacket is thus represented by amplitudes at grid points. The changes in amplitudes with time are determined by the action of the time-evolution operator on the wavepacket. The time-evolution operator $U(t) = \exp\{-i\hat{H}t/\hbar\}$ contains the Hamiltonian, $\hat{H}$. Applying the time-evolution operator to the wavepacket therefore requires evaluating the action of the Hamiltonian on the wavepacket. The Hamiltonian has a potential part and a kinetic part. The action of the potential on the wavepacket merely involves a multiplication while the action of the kinetic part involves second derivatives. These can be efficiently handled in a variety of ways [50].

In this section, the generally used numerical methods for quantum wavepacket simulation are shown by reference to [49–51].

2.5.1 Representation

The starting point of discussion is the TD Schrödinger equation:

$$H\Psi(x,t) = i\hbar\frac{\partial\Psi(x,t)}{\partial t}, \tag{2.59}$$

where H is the Hamiltonian operator, being time-dependent or time-independent, and $\Psi(x,t)$ is the TD wavefunction. The central task of this section is to find the numerical solution for $\Psi(x,t)$ that contains all the necessary dynamical information of the system. For a time-independent Hamiltonian, the solution to the TD Schrödinger equation may be expressed as

$$\Psi(x,t) = \exp(-iHt/\hbar)\Psi(x,0). \tag{2.60}$$

Thus, the action of the time-evolution operator $\exp(-iHt/\hbar)$ on the wavefunction $\Psi(t)$ has to be evaluated in the propagation.

2.5.2 Initial condition

The initial wavepacket is placed on the chosen grid. The initial form of the wavepacket is often chosen to be of Gaussian shape in the scattering coordinate:

$$\Psi(x,t=0) = N\exp(-ik_0x - (x-x_0)^2/4\sigma^2), \tag{2.61}$$

where k_0 is the average momentum of the wavepacket and σ is its width. The normalization constant is $N = (2\pi\sigma^2)^{-1/4}$. A Gaussian wavepacket remains Gaussian with its center traveling at the classical speed and the width of the wavepacket spreads even in the absence of an interaction potential.

2.5.3 Expansion by eigenfunction of the system

For a time independent Hamiltonian, a wavepacket can be propagated trivially in terms of the eigenstates of $H, \{\phi_n\}$. For scattering wavepackets these eigenstate must span a region in the scattering coordinate that covers the interaction and non-interaction regions. In terms of this set of eigenstates the time-evolved wavepacket is given by

$$|\Psi(t)\rangle = \exp\left(-\frac{i}{\hbar}Ht\right)|\Psi(0)\rangle = \sum_n C_n \exp\left(-\frac{i}{\hbar}E_n t\right)|\phi_n\rangle, \tag{2.62}$$

where the time-independent coefficients C_n are given by

$$C_n = \langle\phi_n|\Psi(0)\rangle, \tag{2.63}$$

and where E_n are the eigenvalues of H. This procedure is straightforward and can be used to obtain the wavepacket at any time t. In addition, it is easy to propagate different initial packets $\Psi(0)$ corresponding, for example, to different initial quantum states of reactants in a reactive scattering calculation. Of course, the computational effort in obtaining the eigenfunctions and eigenvalues of H can be very significant, even prohibit. The diagonalization of Hamiltonian matrix H scales exponentially with system dimension and therefore diagonaization in multidimension becomes formidable

task.

If we use the method in expansion by Eigenfunction of the system, we must get eigenfunction of the system beforehand. In order to obtain eigenfunction of the system, we can simply discretize the time-independent Schrödinger equation and put it into matrix form, which can then be numerically solved. For the one dimensional case, the time-independent Schrödinger equation at each point along x can be written as

$$-\frac{\hbar^2}{2m}\left(\frac{d^2\phi}{dx^2}\right)_{x_n} + V(x_n)\phi_{x_n} = E\phi_{x_n}. \tag{2.64}$$

Now using the basic finite difference approximation,

$$\left(\frac{d^2\phi(x)}{dx\phi^2}\right)_{x_n} = \frac{\phi_{x_{n+1}} - 2\phi_{x_n} + \phi_{x_{n-1}}}{(\Delta x)^2}, \tag{2.65}$$

where Δx is the spatial interval spacing, we can write Eq. (2.64) as

$$k(2\phi_{x_n} - \phi_{x_{n+1}} - \phi_{x_{n-1}}) + V(x_n)\phi_{x_n} = E\phi_{x_n}, \tag{2.66}$$

where $k = \frac{\hbar^2}{2m(\Delta x)^2}$. This can be written in matrix form as

$$\begin{pmatrix} 2k & -k & 0 & 0 & 0 & \cdots \\ -k & 2k & -k & 0 & 0 & \cdots \\ \cdots & \cdots & \cdots & \cdots & \cdots & \cdots \\ \cdots & 0 & 0 & -k & 2k & -k \\ \cdots & 0 & 0 & 0 & -k & 2k \end{pmatrix} \begin{pmatrix} \phi_{x_1} \\ \phi_{x_2} \\ \phi_{x_3} \\ \cdots \\ \phi_{x_{N-1}} \\ \phi_{x_N} \end{pmatrix} +$$

$$\begin{pmatrix} V(x_1) & 0 & 0 & 0 & 0 & \cdots \\ 0 & V(x_2) & 0 & 0 & 0 & \cdots \\ 0 & 0 & V(x_2) & 0 & 0 & \cdots \\ \cdots & \cdots & \cdots & \cdots & \cdots & \cdots \\ \cdots & 0 & 0 & 0 & V(x_{N-1}) & 0 \\ \cdots & 0 & 0 & 0 & 0 & V(x_N) \end{pmatrix} \begin{pmatrix} \phi_{x_1} \\ \phi_{x_2} \\ \phi_{x_3} \\ \cdots \\ \phi_{x_{N-1}} \\ \phi_{x_N} \end{pmatrix} = E \begin{pmatrix} \phi_{x_1} \\ \phi_{x_2} \\ \phi_{x_3} \\ \cdots \\ \phi_{x_{N-1}} \\ \phi_{x_N} \end{pmatrix}. \tag{2.67}$$

This eigenvalue problem can be solved numerically, and the corresponding eigenvectors can be found. But the task of finding the eigenfunction is formidable when we consider many dimensional systems. When we use N grid points per one degree of freedom,

we must diagonalize $N \times N, N^2 \times N^2$, and $N^3 \times N^3$ Hamiltonian matrix, in one, two and three dimensional systems, respectively. Because of this exponential scaling of the computational cost with respect to the dimension, we cannot apply this method to many dimensional systems.

2.5.4 Finite difference method

Solving Eq. (2.59) for a given initial wavefunction $\Psi(0)$ constitutes a time propagation of the wavefunction, which is carried out by integrating the wavefunction in time. The propagation can be accomplished by using a variety of integration methods. The most straightforward approach is based on finite difference schemes including the Runge-Kutta method, second order difference (SOD) method, or higher order difference methods. At present, however, more sophisticated methods, such as the split-operator method, are often used in practical applications.

In the SOD method, one approximates the time-derivative of the wave function by second-order finite differencing:

$$\frac{\partial}{\partial t}\Psi(t) = \frac{\Psi(t+\Delta) - \Psi(t-\Delta)}{2\Delta} + O(\Delta^2), \tag{2.68}$$

which results in the following iterative formula for the wavefunction:

$$\Psi(t+\Delta) = \Psi(t-\Delta) - 2\frac{i}{\hbar}\Delta H\Psi(t). \tag{2.69}$$

The wavefunction obtained by the SOD method of Eq. (2.69) is correct to second order $O(\Delta^2)$. Since the iterative procedure in Eq. (2.69) requires wavefunctions at two prior times, Ψ_0 and Ψ_1, the SOD method requires the use of a self-starting scheme such as the Runge-Kutta method to generate Ψ_1 first. The SOD method is stable with respect to the time increment Δ below a certain critical value $\Delta_{\max}$. If the step size Δ is greater than $\Delta_{\max}$, the solution becomes unstable and increases exponentially (blow-up). The SOD method is extremely easy to use but is not very efficient for large scale calculations because it generally requires the small time step in order to obtain stable and accurate solutions.

2.5.5 Split-Operator method

The kinetic energy operator in the Hamiltonian contains one or more second derivatives, which are to act on the wavepacket. In the Fourier transform method, this is done by first Fourier transforming the wavefunction $\Psi(x)$ to the momentum representation and thereafter multiplying each momentum component by $-k^2$. Here k is the wavenumber.

Finally, the resulting function is transformed back to the original coordinate representation. We illustrate this in one dimension by writing

$$\Psi(k) = \frac{1}{\sqrt{2\pi}} \int_{-\infty}^{+\infty} \Psi(x) \exp\{-ikx\} dx = FT[\Psi(x)], \tag{2.70}$$

and

$$\Psi(x) = \frac{1}{\sqrt{2\pi}} \int_{-\infty}^{+\infty} \Psi(k) \exp\{ikx\} dk = FT^{-}[\Psi(k)], \tag{2.71}$$

whereby

$$\frac{\Psi(x)}{dx} = \frac{1}{\sqrt{2\pi}} \int_{-\infty}^{+\infty} ik\Psi(k) \exp\{ikx\} dk = FT^{-}[ik\Psi(k)], \tag{2.72}$$

and thus

$$\frac{d^2\Psi(x)}{dx^2} = -\frac{1}{\sqrt{2\pi}} \int_{-\infty}^{+\infty} k^2\Psi(k) \exp\{ikx\} dk = FT^{-}[-k^2\Psi(k)]. \tag{2.73}$$

The split-operator (SO) propagator splits the kinetic energy operator $\hat{T}$ and the potential energy operator $\hat{V}$ into different exponentials when applying the time-evolution operator. Since $\hat{T}$ and $\hat{V}$ do not commute this is an approximation. The splitting can be performed so that the kinetic energy operator is sandwiched between potential energy operators. This is referred to as the kinetic referenced SO method. Alternatively the potential energy operator is sandwiched between kinetic energy operators, giving

the potential referenced SO method.

Choosing a time-step Δt and neglecting the non-commutativity, the potential referenced SOP can be written

$$\exp\left(-\frac{i\Delta t\hat{H}}{\hbar}\right) \approx \exp\left(-\frac{i\Delta t\hat{T}}{2\hbar}\right)\exp\left(-\frac{i\Delta t\hat{V}}{\hbar}\right)\exp\left(-\frac{i\Delta t\hat{T}}{2\hbar}\right) + O((\Delta t)^3). \quad (2.74)$$

By making Δt suitably small, the propagation

$$\Psi(t+\Delta t) = \exp\left(-\frac{i\Delta t\hat{T}}{2\hbar}\right)\exp\left(-\frac{i\Delta t\hat{V}}{\hbar}\right)\exp\left(-\frac{i\Delta t\hat{T}}{2\hbar}\right)\Psi(t) \quad (2.75)$$

becomes accurate. The SO propagator is unitary and therefore numerically stable as it conserves the norm of the wavefunction.

The potential referenced SO propagation begins with a Fourier transformation of the wavefunction to momentum space. According to Eq. (2.73), it is then multiplied by $\exp(-ik^2\Delta t\hbar/4\mu)$, where μ is a reduced mass. Thereafter it is transformed back to coordinate space and multiplied by $\exp(-i\Delta tV/\hbar)$ using Eq. (2.71). Finally another Fourier transform to momentum space, multiplication by $\exp(-ik^2\Delta t\hbar/4\mu)$ and back transformation are carried out.

The actions of the kinetic energy operator can be combined with the adjacent timestep, thereby reducing the number of required Fourier transforms. The fast Fourier

transform (FFT) method is a numerically efficient implementation of the discrete Fourier transform which scales as $O(N \ln N)$, where N is the number of grid points. Therefore practical implementation of the SO propagation requires the use of the FFT method, so that the actions of the operators will be evaluated in their respective local representations.

2.6 Quantum theory of chemical reaction

In this section the quantum theories of chemical reactions are discussed. Especially reactive scattering theory, rate constant using the reaction probability, and transition state theory which is not rigorous quantum theory, are explained. Reactive scattering deals with rearrangement of particles such as an approach of reactants, a rearrangement of the atoms, and a separation of the products, which is at the heart of chemical reactions. The exact thermal rate constant for an elementary bimolecular reaction can be rigorously calculated by Boltzmann averaging the reactive flux over the initial states and the collision energy. On the other hand, for transition state theory the rate constant, which is widely applicable in the gas phase, is derived by assumption of a special type of chemical equilibrium. Since a more detailed description of these theories is given in Ref. [50, 51], the outline is discussed in this section.

2.6.1 Wavepacket correlation function formulation of reactive scattering

Scattering theory in general, and reactive scattering in particular, are very easy to grasp intuitively using a time-dependent approach. A wavepacket corresponding to a well-defined internal state of reactant states enters the interaction region and bifurcates: part returns to reactants and part proceeds to different product arrangements. The projection of the product wavepacket onto the asymptotic eigenstates of products gives the various transition amplitudes from the initial states to all final states, i.e., a column of the scattering matrix (S-matrix).

In reactive scattering, since the final chemical arrangement of the atoms in the product states is different from that in the reactants, we will need to consider scattering eigenstates corresponding to multiple chemical arrangements. We will be interested in incoming eigenstates with well-defined boundary conditions in the reactant arrangement channel, and outgoing eigenstates with well-defined boundary conditions in the product arrangement channel. The S-matrix will then be defined in terms of the overlap of degenerate scattering eigenstates with these different boundary conditions.

We consider a wevepacket located at the asymptotic reactant channel having a momentum of incoming direction initially and propagated to the interaction scattering

region. The transition amplitude from an incoming state to an outgoing state, which represents the S-matrix elements, is defined by the overlap between scattering eigenstates corresponding to incoming and outgoing boundary conditions. The amplitude is then written as

$$S_{\beta,\alpha}(E)\delta(E - E^{'}) = \langle \psi_{\beta}^{-}(E^{'})|\psi_{\alpha}^{+}(E)\rangle. \tag{2.76}$$

where α and β represent the initial and final arrangement channels, respectively, ψ_{α}^{+} is the incoming eigenstate, and ψ_{β}^{-} is outgoing eigenstate. The energy-normalized incoming scattering eigenstate takes the form:

$$\psi_{\alpha}^{+}(E) = \frac{1}{2\pi\hbar\eta_{\alpha}(E)} \int_{-\infty}^{\infty} e^{-iHt/\hbar}\phi_{\alpha}^{+}e^{iEt/\hbar}dt, \tag{2.77}$$

where $\eta_{\alpha}(E)$ is the coefficient of the energy-normalized eigenstate $\psi_{\alpha}^{+}(E)$ contained in ϕ_{α}^{+}. Similarly, the energy-normalized outgoing eigenstate is then given by

$$\psi_{\beta}^{-}(E') = \frac{1}{2\pi\hbar\eta_{\beta}(E')} \int_{-\infty}^{\infty} e^{-iHt/\hbar}\phi_{\beta}^{-}e^{iE't/\hbar}dt, \tag{2.78}$$

where $\eta_{\beta}(E')$ is the coefficient of the energy-normalized eigenstate $\psi_{\beta}^{-}(E')$ contained in ϕ_{β}^{-}.

From Eq. (2.76), the S-matrix is then simply related to the overlap between these

two energy-normalized eigenfunctions:

$$S_{\beta,\alpha}(E)\delta(E-E') = \langle\psi_\beta(E')|S|\psi_\alpha(E)\rangle = \langle\psi_\beta^-(E')|\psi_\alpha^+(E). \tag{2.79}$$

Substituting Eqs. (2.77) and (2.78) into Eq. (2.79), we obtain

$$\begin{aligned} & S_{\beta,\alpha}(E)\delta(E-E') \qquad (2.80)\\ &= \frac{(2\pi\hbar)^{-2}}{\eta_\beta^*(E')\eta_\alpha(E)} \int_{-\infty}^{\infty}\int_{-\infty}^{\infty} \langle\phi_\beta^-|e^{-iH(t'-t'')/\hbar}|\phi_\alpha^+\rangle e^{iE_+(t'-t'')/\hbar} e^{iE_-(t'+t'')/\hbar} dt'dt'' \\ &= \frac{(2\pi\hbar)^{-2}}{\eta_\beta^*(E')\eta_\alpha(E)} \int_{-\infty}^{\infty} \langle\phi_\beta^-|e^{-iHt/\hbar}|\phi_\alpha^+\rangle e^{iEt/\hbar} dt. \end{aligned}$$

Furthermore Tannor and coworkers introduced the new formula of scattering matrix elements [67–75], using Fourier transform of time correlation function, which is equivalent with the following flux-operation formula:

$$|S_{\beta,\alpha}(E)|^2 = \frac{|\int_{-\infty}^{\infty}\langle\phi_\beta^-|e^{-iHt/\hbar}|\phi_\alpha^+\rangle e^{iEt/\hbar}dt|^2}{|\int_{-\infty}^{\infty}\langle\phi_\alpha^+|e^{-iHt/\hbar}|\phi_\alpha^+\rangle e^{iEt/\hbar}dt||\int_{-\infty}^{\infty}\langle\phi_\beta^-|e^{-iHt/\hbar}|\phi_\beta^-\rangle e^{iEt/\hbar}dt|}. \tag{2.81}$$

Therefore reactive scattering transition amplitudes are described from the Fourier transform of the cross correlation between a reactant wavepacket going forward in time and a product wavepacket going backword in time.

2.6.2 Rate constant using cumulative reaction probability

The reaction probability may be defined at different levels of detail. Complete information about the scattering process requires knowledge of all the individual S-matrix elements, $\{S_{\beta\alpha}(E)\}$. Some state-averaged quantities are of relevance, such as the initial (final) state-selected total reaction probability

$$N_{\alpha(\beta)}(E) = \sum_{\alpha(\beta)} |S_{\beta,\alpha}(E)|^2, \tag{2.82}$$

or the cumulative reaction probability

$$N(E) = \sum_{\alpha\beta} |S_{\beta,\alpha}(E)|^2. \tag{2.83}$$

It is the cumulative reaction probability, which gives the thermal reaction rate constant averaged over the energy distribution:

$$k(T) = \frac{1}{2\pi\hbar Q(T)} \int_0^\infty N(E) e^{-E/k_B T} dE, \tag{2.84}$$

where $Q(T)$ is the reactant partition function. From the practical point of view it is advantageous to find the total or cumulative reaction probabilities directly without explicit reference to the state-to-sate probabilities.

Chapter 3

Construction of Diabatic Potential for Proton Transfer in Molecular Pairs

In this chapter a construction method of potential energy surface (PES) in diabatic picture for intermolecular proton transfer is discussed. This chapter is focused on the proton-bonded ammonia (AmH^+-Am) and imidazole (ImH^+-Im) pairs as homo-molecular proton transfer systems and on the proton-bonded imidazole-ammonia (ImH^+-Am) and ammonia-water (AmH^+-Wat) pairs as hetero-molecular systems. In the following, the specific introduction of this chapter is explained in section 1; theoretical background and computational methods are explained in section 2; results and discussion are explained in section 3; and finally conclusion of this chapter is explained in section 4.

3.1 Introduction

Most approaches to chemical reactions analyze the PES by quantum chemical calculations derived under the Born-Oppenheimer approximation, also known as the adiabatic PES. Although quantum chemical calculations are becoming possible for large molecular systems, accurate PES calculations for understanding chemical reaction tend to be unfeasible. In addition, tough analytical function for PES requires to analyze the reaction, the global function has not been known.

Rather than examine the adiabatic PES, another approach to chemical reactions is to analyze the diabatic PES. In contrast to the adiabatic PES, the diabatic PES presents electronic states that change constantly to confine the eigenstates of the electronic Hamiltonian. There are some approaches to describing the diabatic potential [4], constructing using some valence bond (VB) electronic wave functions [5–8]. Especially, empirical valence bond (EVB) [9] or multistate empirical valence bond (MS-EVB) [10] approach extended EVB is used the molecular mechanical functions to construct the PES and applied to the molecular dynamics (MD) simulations for many proton transfer systems [11–27]. To basic idea, consider a two-state VB electronic wave function as the diabatic basis:

$$|\psi\rangle = c_1|\phi_1\rangle + c_2|\phi_2\rangle, \tag{3.1}$$

where $|\phi_1\rangle$ and $|\phi_2\rangle$ are VB wave functions that describes the electronic structure of the reactant (RS) and product states (PS), respectively. As discussed in chapter 2, the lowest adiabatic potential energy $V^{\rm ad}$ is then given by the lower root of the 2×2 secular equation; specifically

$$V^{\rm ad} = \frac{V_{11}^{\rm di} + V_{22}^{\rm di}}{2} - \sqrt{\left(\frac{V_{11}^{\rm di} - V_{22}^{\rm di}}{2}\right)^2 + V_{12}^{\rm di 2}}, \tag{3.2}$$

where

$$V_{11}^{\rm di} = \langle\phi_1|H|\phi_1\rangle, \tag{3.3}$$

$$V_{22}^{\rm di} = \langle\phi_2|H|\phi_2\rangle, \tag{3.4}$$

$$V_{12}^{\rm di} = \langle\phi_2|H|\phi_1\rangle, \tag{3.5}$$

$V_{11}^{\rm di}$ and $V_{22}^{\rm di}$ are the potential energies for the two VB structures of the RS and PS, respectively. In this approach $V_{11}^{\rm di}$, $V_{22}^{\rm di}$, and $V_{12}^{\rm di}$ function forms including parameters can be obtained to fit in experimental or ab initio data. In these works, $V_{11}^{\rm di}$ and $V_{22}^{\rm di}$ are related to use of molecular mechanics potential functions, especially, which are taken as the harmonic normal-mode potential or Morse potential [12, 13, 15, 16, 23, 24]. On the other hand, although the selection of $V_{12}^{\rm di}$ is less obvious, Gaussian

function as V_{12}^{di} proposed by Chang and Millar [12] has been widely used. However, they did not be confirmed whether the obtained diabatic potentials produce the reliable adiabatic potentials or not, although these functions are obtained to fit in some data. In addition, to obtain these analytical functions including parameters uniquely using fewer information is an important task to apply widely to describing the chemical reactions. Therefore, a proposal of simple method for light or more uniquely construction of the diabatic potentials (V_{11}^{di} and V_{22}^{di}) and non-diagonal matrix element (V_{12}^{di}) using the analytical functions is important to analyze the chemical reaction and it can be widely applied to describing the large molecular systems such as proteins.

In this chapter, a simple construction method of global PES for intermolecular proton transfer by use of Morse potential as V_{11}^{di} and V_{22}^{di}, and Gaussian function as V_{12}^{di} in diabatic potential matrix is suggested, and the validity to use these potential functions is confirmed. Here, we focus on the (a) AmH^+-Am and (b) ImH^+-Im pairs as homo-molecular proton transfer systems and on the (c) ImH^+-Am and (d) AmH^+-Wat pairs as hetero-molecular systems, the structures of which are shown in Fig. 3.1. We investigate the portability to use the Morse potential and Gaussian function as the diabatic potential matrix elemetns by comparison of the transformed adiabatic potential from the diabatic one and the calculated by DFT calculation in these systems. Finally, we discuss the proton transfer characters using obtained V_{11}^{di}, V_{22}^{di}, and V_{12}^{di} for homo-

and hetero-molecular pairs.

3.2 Theoretical and calculation methods

3.2.1 Calculation models

In the construction of PES for proton transfer, the four proton transfer models were focused: (a) AmH^+-Am, (b) ImH^+-Im as homo-molecular pairs, and (c) ImH^+-Am, (d) AmH^+-Wat as hetero-molecular pairs (Fig. 3.1). Figure 3.2 shows also these models and PES coordinates. For homo-molecular pairs, coordinate R denotes the intermolecular distance and x is the translating proton position, which is defined as a displacement from the center of the intermolecular distance. For hetero-molecular pairs, r is used as the displacement between a proton-bonded atom and the proton.

3.2.2 Diabatic potential functions (V_{11}^{di}, V_{22}^{di} and V_{12}^{di})

In this chapter, for the proton transfer models, the PES of proton transfer were constructed by using diabatic picture. Diabatic PES can be constructed using a variety of VB configurations [4–8]. Here, we considered a two-state VB electronic wave function as the diabatic basis corresponding to the RS and PS, i.e., Eq. (3.1). In particular, the EVB approach can be related to use of molecular mechanical potential functions de-

scribing the molecular vibration, which is rational for understanding chemical reaction. In most cases, the diagonal matrix elements ($V_{11}^{\rm di}$ and $V_{22}^{\rm di}$) are taken as the harmonic normal-mode or Morse potentials [12, 13, 15, 16, 23, 24]. On the other hand, Chang and Millar [12] suggested the use of a generalized Gaussian function as the non-diagonal matrix element ($V_{12}^{\rm di}$).

Therefore, we selected the Morse function as the $V_{11}^{\rm di}$ and $V_{22}^{\rm di}$, and Gaussian function as the $V_{12}^{\rm di}$ to construct PES for proton transfer. For homo-molecular pairs, $V_{11}^{\rm di}$, $V_{22}^{\rm di}$ and $V_{12}^{\rm di}$ are explicitly defined as

$$V_{11}^{\rm di}(x;R) = D(1-e^{-k(x+x_0)})^2 + c, \tag{3.6}$$

$$V_{22}^{\rm di}(x;R) = D(1-e^{k(x-x_0)})^2 + c, \tag{3.7}$$

$$V_{12}^{\rm di}(x;R) = A\exp(-bx^2). \tag{3.8}$$

For hetero-molecular pairs, $V_{11}^{\rm di}$, $V_{22}^{\rm di}$ and $V_{12}^{\rm di}$ are defined as

$$V_{11}^{\rm di}(r;R) = D_1(1-e^{-k_1(r-r_0)})^2 + c, \tag{3.9}$$

$$V_{22}^{\rm di}(r;R) = D_2(1-e^{-k_2(R-r-r_0')})^2 + c + D_3, \tag{3.10}$$

$$V_{12}^{\rm di}(r;R) = A\exp(-b(r-r_c)^2). \tag{3.11}$$

The PES was constructed by optimization of the potential parameters in these functions (V_{11}^{di}, V_{22}^{di} and V_{12}^{di}). For V_{11}^{di} and V_{22}^{di}, the parameters D, D_1, and D_2 are binding energies; x_0, r_0, r_0' are the equilibrium bond lengths; k, k_1, and k_2 are the decay constants. For V_{12}^{di}, parameter A is the amplitude of the Gaussian function, parameter b corresponds to the spread of the function, and r_c is the point of the maximum value of the function.

3.2.3 Optimization of potential parameters

Optimization of the potential parameters was conducted according to the following procedures.

First, we estimated the parameters of V_{11}^{di} and V_{22}^{di}. Parameters D, D_1, and D_2 were estimated by dissociation energy of the proton corresponding to one side of the molecular pairs, i.e., ammonium, imidazolium, and oxonium ions. x_0, r_0, r_0' were used the equilibrium bond lengths of these molecules. The estimated values of these parameters are shown in Table 3.1. For hetero-molecular pairs, parameter D_3 was obtained from the difference between $V^{\mathrm{ad}}(r_0; R)$ and $V^{\mathrm{ad}}(r_0'; R)$:

$$D_3 = V^{\mathrm{ad}}(r_0'; R) - V^{\mathrm{ad}}(r_0; R). \tag{3.12}$$

The remaining parameters k, k_1, and k_2 included in V_{11}^{di} and V_{22}^{di} are considered to be

dependent on the R coordinate. These parameters were estimated by comparison with the adiabatic potential obtained from DFT calculations according to Eq. (3.2). V_{11}^{di} and V_{22}^{di} describes molecular vibration for the RS and PS, respectively. Therefore, we assumed that V_{11}^{di} and V_{22}^{di} reproduced the adiabatic potential, when the proton position was closer to a binding atom than a stable point ($r < r_0$). Here, the parameter k was estimated by comparing with the V_{12}^{di} and adiabatic potential at $x = 2x_0$ for homo-molecular pairs for fixed R. In the same way, for hetero-molecular pairs, k_1 and k_2 were determined by comparing with the adiabatic potential at $r = 2r_0 - R/2 \equiv r_{k_1}$ and $r = 3R/2 - 2r_0' \equiv r_{k_2}$, respectively, for fixed R. These relations are explicitly defined as

$$V_{22}^{\mathrm{di}}(2x_0) = V^{\mathrm{ad}}(2x_0), \tag{3.13}$$

$$V_{11}^{\mathrm{di}}(r_{k_1}) = V^{\mathrm{ad}}(r_{k_1}), \tag{3.14}$$

$$V_{22}^{\mathrm{di}}(r_{k_2}) = V^{\mathrm{ad}}(r_{k_2}). \tag{3.15}$$

for homo- and hetero-molecular pairs, respectively. Parameters k, k_1, and k_2 are then

denoted as

$$k = \frac{1}{x_0} \ln \left(1 + \sqrt{\frac{V^{\mathrm{ad}}(2x_0) - c}{D}} \right), \tag{3.16}$$

$$k_1 = \frac{1}{r_0 - r_{k_1}} \ln \left(1 + \sqrt{\frac{V^{\mathrm{ad}}(r_{k_1}) - c}{D_1}} \right), \tag{3.17}$$

$$k_2 = \frac{1}{r_{k_2} + r'_0 - R} \ln \left(1 + \sqrt{\frac{V^{\mathrm{ad}}(r_{k_2}) - c - D_3}{D_2}} \right). \tag{3.18}$$

Subsequently, parameters A and b of V_{12}^{di} depending on the coordinate R were estimated. These parameters were also estimated by comparison with the adiabatic potential obtained from DFT calculations and using obtained diabatic potentials (V_{11}^{di} and V_{22}^{di}). Determination of these parameters was conducted according to the following steps for each pairs.

First, parameter A was estimated. Because this parameter represents the amplitude of the Gaussian type function, parameter b vanishes at $x = 0$ for homo-molecular pairs. Thus, the relationship between the adiabatic and diabatic potentials at $x = 0$ and fixed R is given by

$$\frac{V_{11}^{\mathrm{di}}(0) + V_{22}^{\mathrm{di}}(0)}{2} - \sqrt{\left(\frac{V_{11}^{\mathrm{di}}(0) - V_{22}^{\mathrm{di}}(0)}{2} \right)^2 + {V_{12}^{\mathrm{di}}}^2(0)} = V^{\mathrm{ad}}(0). \tag{3.19}$$

Parameter A was then estimated by using obtained V_{11}^{di} and V_{22}^{di}, which was expressed

as

$$A = V_{11}^{\mathrm{di}}(0) - V^{\mathrm{ad}}(0), \tag{3.20}$$

for homo-molecular pairs. For hetero-molecular pair, parameter A was estimated at the cross point ($r = r_c$) of V_{11}^{di} and V_{22}^{di} substituted $D_3 = 0$. Parameter A was then expressed as

$$A = V_{11}^{\mathrm{di}}(r_c) - V^{\mathrm{ad}}(r_c), \tag{3.21}$$

for hetero-molecular pairs.

Next, the remaining parameter b of V_{12}^{di} was estimated. This parameter corresponds to the spread of the Gaussian type function. For homo-molecular pair, the midpoint between the local minimum (x_0) and local maximum ($x = 0$) is assumed to define the spread of V_{12}^{di}. Therefore, the relationship between the adiabatic and diabatic potentials at $x = x_0/2$ and fixed R is also given by

$$\frac{V_{11}^{\mathrm{di}}(\frac{x_0}{2}) + V_{22}^{\mathrm{di}}(\frac{x_0}{2})}{2} - \sqrt{\left(\frac{V_{11}^{\mathrm{di}}(\frac{x_0}{2}) - V_{22}^{\mathrm{di}}(\frac{x_0}{2})}{2}\right)^2 + V_{12}^{\mathrm{di}^2}\left(\frac{x_0}{2}\right)} = V^{\mathrm{ad}}\left(\frac{x_0}{2}\right). \tag{3.22}$$

According to this relation, parameter b is expressly defined by

$$b = \frac{2}{x_0^2}\left[\ln A^2 - \ln\left\{\left(\frac{V_{11}^{\rm di}(\frac{x_0}{2}) + V_{22}^{\rm di}(\frac{x_0}{2})}{2} - V^{\rm ad}\left(\frac{x_0}{2}\right)\right)^2 - \left(\frac{V_{11}^{\rm di}(\frac{x_0}{2}) - V_{22}^{\rm di}(\frac{x_0}{2})}{2}\right)^2\right\}\right]. \tag{3.23}$$

In the same way, for hetero-molecular pairs, b was determined by comparing with the adiabatic potential at $r = (r_c + r_0)/2 \equiv r_b$ for fixed R, which was defined by

$$b = \frac{1}{(r_b - r_c)^2}\left[\ln A^2 - \frac{1}{2}\ln\left\{\left(\frac{V_{11}^{\rm di}(r_b) + V_{22}^{\rm di}(r_b)}{2} - V^{\rm ad}(r_b)\right)^2 - \left(\frac{V_{11}^{\rm di}(r_b) - V_{22}^{\rm di}(r_b)}{2}\right)^2\right\}\right]. \tag{3.24}$$

3.2.4 Adiabatic potential energy calculation

To obtain the adiabatic PES $V^{\rm ad}(x, R)$ or $V^{\rm ad}(r, R)$ for the proton transfer reaction, quantum chemical calculations were performed with stepwise movement of the proton and intermolecular distances by 0.02 and 0.05 Å, respectively. The geometries of the molecules were then kept in the minimum energy structures, except for the proton position (x or r) and the intermolecular distance (R). Minimum energy structures, as shown in Fig. 3.1, were determined by geometrical optimization. Finally, the adiabatic potential energies were fitted using a polynomial series function of the fourth order with respect to x or r, and of the third order with respect to R [52, 53]. In the previous

works [54, 55], the proton transfer of ImH^+-Im systems was discussed with the B3LYP approach. Therefore, all DFT calculations were performed at the B3LYP/aug-cc-pVDZ level using the Gaussian-09 package [56].

3.3 Results and Discussion

First the potential parameters k, k_1, k_2, and D_3 of $V_{11}^{\rm di}$ and $V_{22}^{\rm di}$ were estimated using Eqs. (3.12) and (3.16)-(3.18) and obtained parameters (Table 3.1) for (a) AmH^+-Am, (b) ImH^+-Im, (c) ImH^+-Am, and (d) AmH^+-Wat. The parameters A and b were then estimated using Eqs. (3.20),(3.21), (3.23), and (3.24). Figure 3.3 shows the computed $V_{11}^{\rm di}$, $V_{22}^{\rm di}$ and $V_{12}^{\rm di}$ values using obtained the potential parameters at some intermolecular distance for (a) AmH^+-Am, (b) ImH^+-Im, (c) ImH^+-Am, and (d) AmH^+-Wat, respectively. To compare with the adiabatic potential by DFT calculation, Figs. 3.4 and 3.5 show the transformed adiabatic potential derived from the diabatic potential matrix elements, $V_{11}^{\rm di}$, $V_{22}^{\rm di}$ and $V_{12}^{\rm di}$, using Eq. (3.2) and one obtained from DFT. Although the potentials using diabatic model not reproduce the ones using DFT around the local minimum of the potentials, however, the figures show that the transformed adiabatic potentials are qualitatively in good agreement with those calculated by DFT calculations for all proton transfer systems at various intermolecular distance R. Thus,

it is indicated that PES for various proton transfer systems can qualitatively reproduce by using V_{11}^{di} and V_{22}^{di} with Morse potential described the vibrational motion and V_{12}^{di} with the Gaussian function by assumption of two-state VB wave functions as a diabatic basis.

In our approach, parameters k, A, and b can be uniquely determined not necessary to fit the potential energy. Especially, the construction procedures of the diabatic potential employed four reference points ($x = x_0, 2x_0, 0$, and $x_0/2$) at fixed R for homo-molecular pairs, while five reference points ($r = r_0, r_{k_1}, r_{k_2}, r_c$, and r_b) for hetero-molecular pairs. Thus, the whole PES of proton transfer are described by using energies of approximately 40 or 50 reference points, while the number of DFT data points to describe the whole adiabatic potential required approximately 500 points. Therefore, the PES describing the entire proton transfer system for diabatic picture can be obtained using less than one-tenth of the reference points required for the adiabatic picture. Furthermore, our method can be applied to proton transfer systems, even when the transition state (TS) cannot be calculated, although the information of TS requires the PES construction in the previous work [12]. Therefore, it is concluded that our construction procedures are appreciate and useful method for construction of PES by using the diabatic picture for the proton transfer systems and can be applied to the large molecular system such as proteins.

Finally, the obtained potential parameters are discussed. Figure 3.6 shows that intermolecular dependence of potential parameter b of V_{12}^{di} for (a) AmH^+-Am, (b) ImH^+-Im, (c) ImH^+-Am, and (d) AmH^+-Wat. The values of parameter b, which describes the spread of the Gaussian function, decreased as R increased. This result indicates that the non-diagonal matrix element (V_{12}^{di}) is broadly distributed along the proton transfer coordinate and the bond mixture between the RS and PS occurs over a wide range, not only at the TS. In addition, because V_{12}^{di} is broadly distributed along the intermolecular distance, proton can be formed mixture between RS and PS and transferred at the location formed hydrogen bond. To clarify the effect of non-diagonal matrix element V_{12}^{di}, the ratio of amplitude for the V_{12}^{di} (parameter A), divided by the crossing point energy of the V_{11}^{di} and V_{22}^{di} was estimated, the results of which were shown in Fig. 3.7. According to Eq. (3.2), V_{12}^{di} contributes to the stability of the adiabatic potential V^{ad}, and the A/V_{11}^{di} ($x = 0$ or $r = r_c$) is assumed to be determined the rate of contribution to the possibility of proton transfer. For both homo-molecular pairs, Fig. 3.7 shows that the values of A/V_{11}^{di} decrease as R increase and are approximately 50 to 80% at various intermolecular distance. Thus, proton can easily transfer at the area formed hydrogen bond for homo-molecular pairs. On the other hand, for both hetero-molecular pairs, the values of A/V_{11}^{di} were constantly about 20% over wide range intermolecular distance, which was lower than homo-molecular pairs for all intermolecular distance. It

indicates that the proton for homo-molecular pairs can transfer easily than for hetero-molecular pairs. From the above discussion, we find that the obtained potentials give the qualitative information about proton transfer even if a simple two-state diabatic model is used.

3.4 Conclusion

PES is an important theoretical approach for understanding chemical reactions. Diabatic potentials are used to understand proton transfer reactions. Especially, EVB approach based on the diabatic picture is used to the molecular mechanical function to construct PES and applied to many applications including molecular dynamics simulation. In this chapter, the PES were constructed based on the diabatic picture for proton transfer models: (a) AmH^+-Am, (b) ImH^+-Im, (c) ImH^+-Am, and (d) AmH^+-Wat. We confirmed that Morse potentials as the diagonal matrix element (V_{11}^{di} and V_{22}^{di}) and Gaussian function as the non-diagonal matrix element (V_{12}^{di}), which are important to apply widely to understanding the chemical reaction including the classical or quantum dynamics simulations, described the proper PES for proton transfer. In addition, we proposed a simple method to uniquely construct the diabatic potentials using these analytical functions. The diabatic potentials at various intermolecular distance were

obtained using fewer reference points than the adiabatic potentials to describe an entire proton transfer system. Therefore, our construction method is useful and can be applied to the large molecular systems such as proteins.

From the values of estimated the potential parameters, the non-diagonal matrix element (V_{12}^{di}) was broadly distributed and the proton-bonded mixture between the RS and PS occurred over a wide range of reaction coordinates, and not only at the TS. Furthermore according to the relation between diagonal and non-diagonal matrix elements, it is found that the proton for homo-molecular pairs can transfer easily than for hetero-molecular pairs.

Table 3.1: Diabatic potential energy parameters for (a) AmH^+-Am, (b) ImH^+-Im, (c) ImH^+-Am, and (d) AmH^+-Wat.

(a) AmH^+-Am		(b) ImH^+-Im	
D(kJ mol^{-1})	r_0(Å)	D(kJ mol^{-1})	r_0(Å)
664.758	1.027	668.81	1.0148
(c) ImH^+-Am			
D_1(kJ mol^{-1})	D_2(kJ mol^{-1})	r_0(Å)	$r_0^{'}$(Å)
668.81	664.758	1.015	1.027
(d) AmH^+-Wat			
D_1(kJ mol^{-1})	D_2(kJ mol^{-1})	r_0(Å)	$r_0^{'}$(Å)
725.69	593.731	1.027	0.977

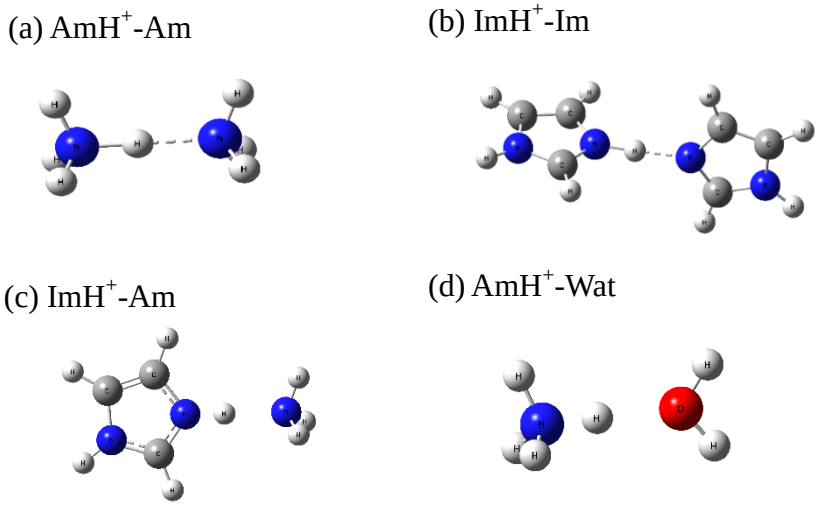

Figure 3.1: Structures of the proton-bonded (a) AmH^+-Am, (b) ImH^+-Im, (c) ImH^+-Am, and (d) AmH^+-Wat pairs.

(a) AmH^+-Am (b) ImH^+-Im

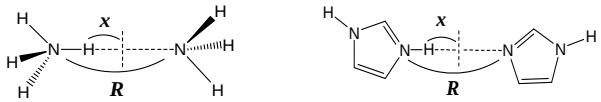

(c) ImH^+-Am (d) AmH^+-Wat

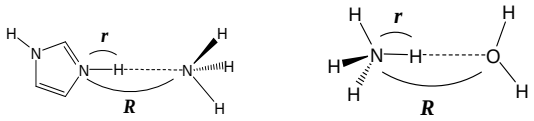

Figure 3.2: Proton transfer model and potential energy coordinates for (a) AmH^+-Am, (b) ImH^+-Im, (c) ImH^+-Am, and (d) AmH^+-Wat.

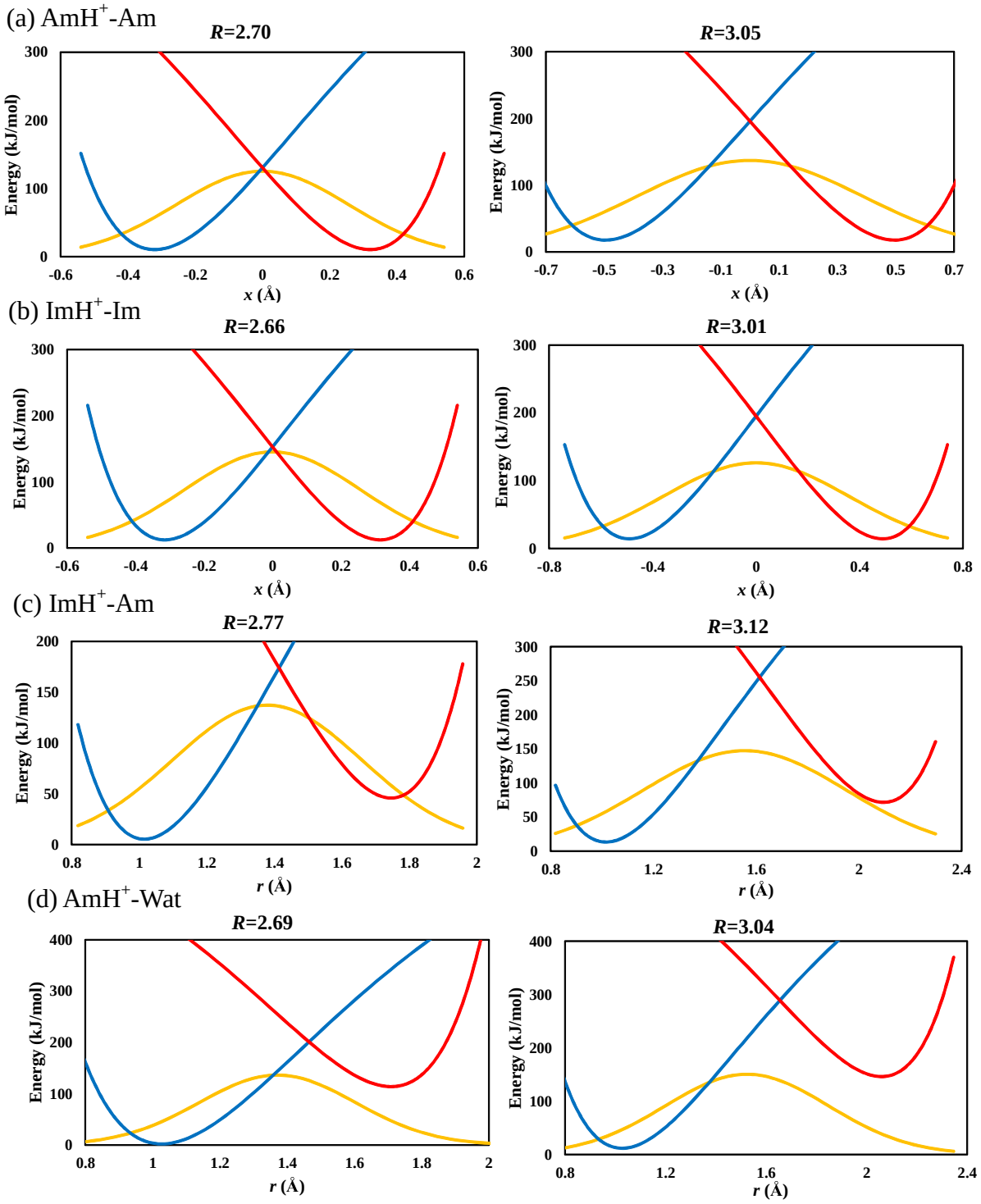

Figure 3.3: Diagonal matrix elements, V_{11}^{di} (blue line) and V_{22}^{di} (red line), and non-diagonal matrix element V_{12}^{di} (yellow line) in diabatic potential matrix computed using obtained potential parameters at some intermolecular distance R for (a) AmH^+-Am, (b) ImH^+-Im, (c) ImH^+-Am, and (d) AmH^+-Wat.

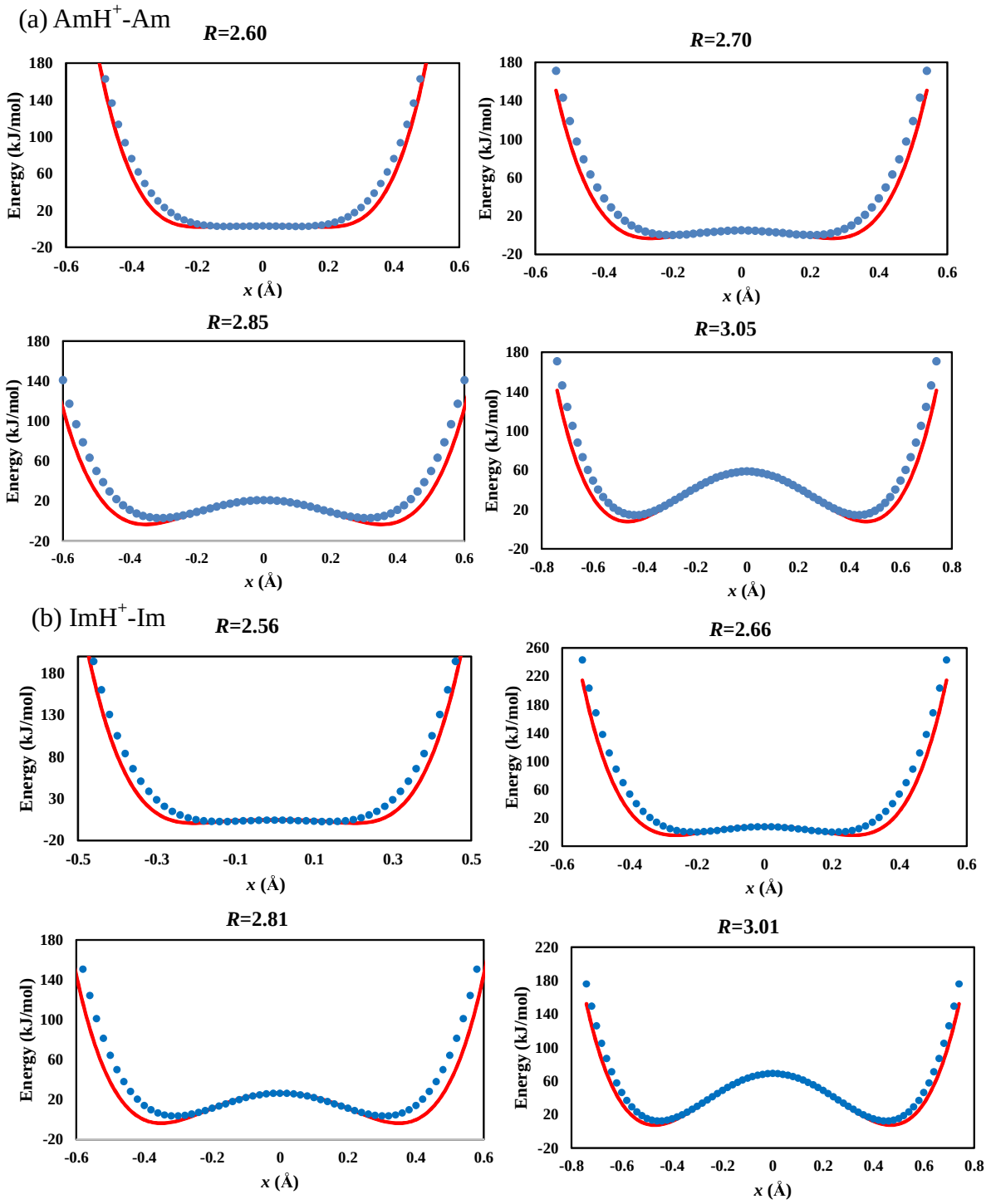

Figure 3.4: Transformed adiabatic potential derived from the diabatic potentials using Eq.(3.2) (red line) and from DFT (blue dots) at some intermolecular distance R for (a) AmH^+-Am, (b) ImH^+-Im.

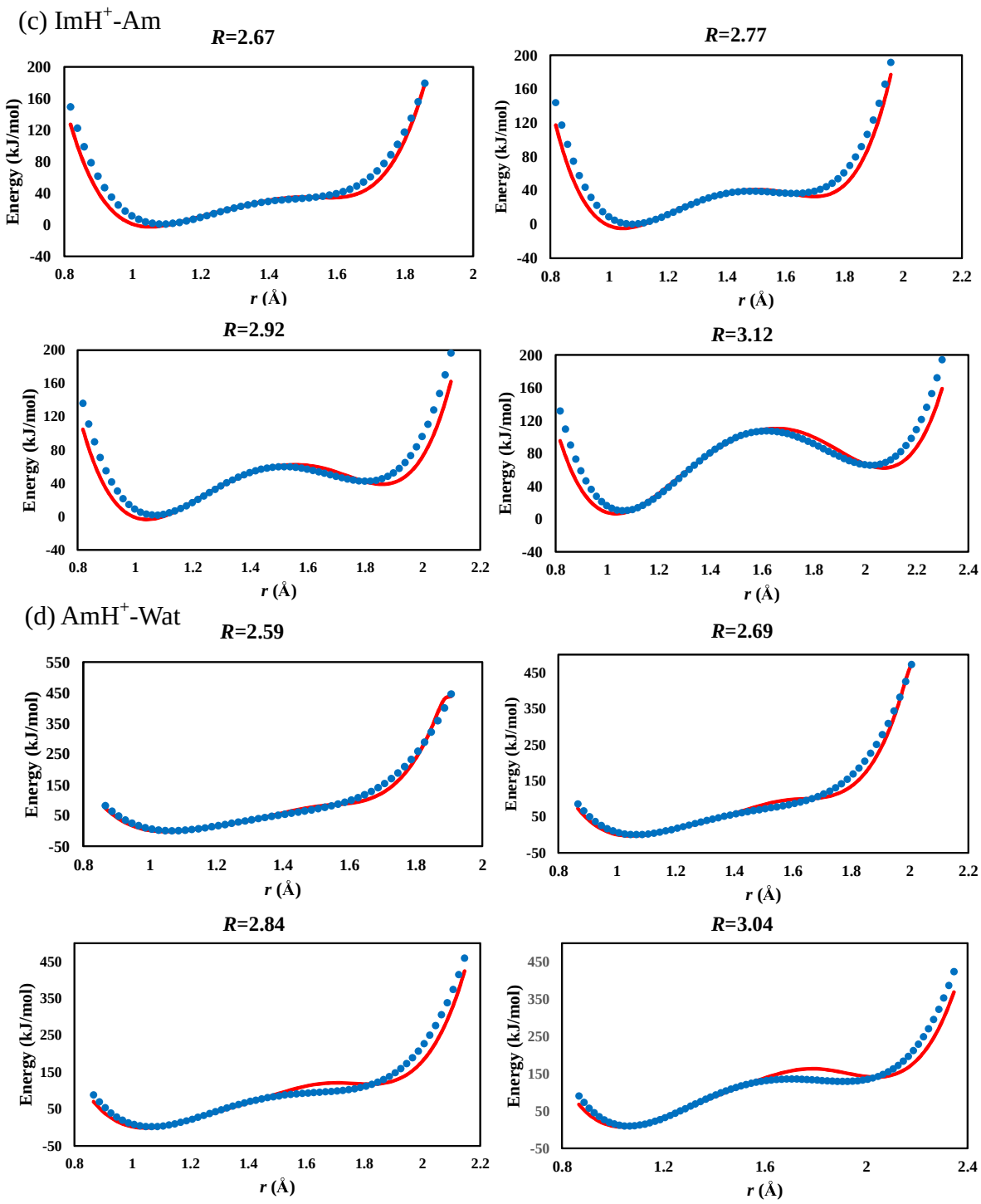

Figure 3.5: Transformed adiabatic potential derived from the diabatic potentials using Eq.(3.2) (red line) and from DFT (blue dots) at some intermolecular distance R for (c) ImH^+-Am, and (d) AmH^+-Wat.

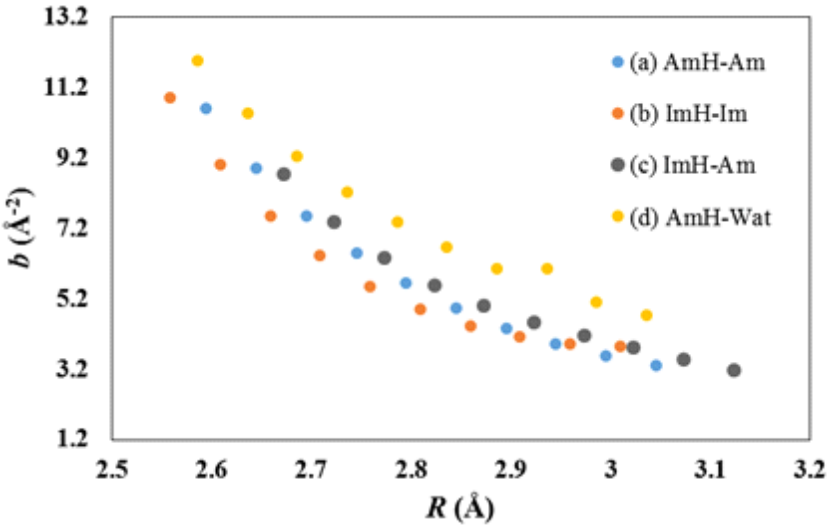

Figure 3.6: Intermolecular dependence of potential parameter b of V_{12}^{di} for (a) AmH^+-Am, (b) ImH^+-Im, (c) ImH^+-Am, and (d) AmH^+-Wat.

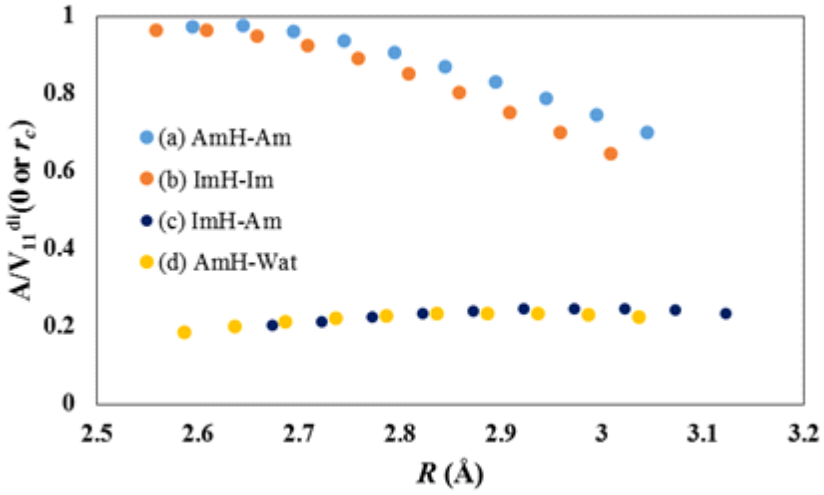

Figure 3.7: Ratio of amplitude for non-diagonal matrix element divided by the crossing point energy of the diabatic potential at $x = 0$ for homo-molecular pairs or $r = r_c$ for hetero-molecular pairs, i.e., A/V_{11}^{di} ($x = 0$ or $r = r_c$).

Chapter 4

Quantum Dynamics Simulation for Rate Constants of Intermolecular Proton Transfer in the Diabatic Picture

In this chapter a method of quantum dynamics simulation for rate constants of intermolecular proton transfer based on the diabatic picture discussed in chapter 3 is discussed. This chapter is focused on the proton-bonded (a) water ($WatH^+$-Wat) and (b) ammonia (AmH^+-Am) pairs as homo-molecular proton transfer systems, and on the (c) ammonia-water (AmH^+-Wat) pairs as hetero-molecular systems. In the following, the specific introduction of this chapter is explained in section 1; theoretical methods are explained in section 2; results and discussion are explained in section 3; and finally conclusion is explained in section 4.

4.1 Introduction

The theoretical study of chemical reactions has been often advanced by following nuclear motions on an adiabatic potential energy surface (PES) obtained from quantum chemical calculations within the Born-Oppenheimer approximation. Reactive scattering studies based on a single electronically adiabatic PES have demonstrated that it is possible to obtain detailed information concerning chemical reactions involving a simple few-atom systems from accurate quantum mechanical calculations [57–66]. The scattering matrix obtained from the quantum scattering calculations, known as the S-matrix, provides the quantum mechanical transition probability amplitudes.

Previously, Tannor et al. [67–71] developed a time-dependent reactive scattering formulation for estimating individual S-matrix elements, and cumulative reaction probabilities have been obtained from time-correlation functions between reactant (RS) and product (PS) wavepackets. Similar time-dependent wave packet formulations have also been introduced and applied by other researchers [72–75]. In these approaches, changes with time are determined by the action of the time-evolution operator on the wavepacket. Several methods to accomplish the time-evolution of wavepacket have been developed [50]. For example, the split-operator, Lanczos, and Chebyshev methods have been successfully used with the time-dependent wavepacket approach. Furthermore, Miller and co-workers have used the reactant partition function to show that the cumu-

lative reaction probability can be directly related to the thermal rate constant [28–30]. Therefore, detailed analyses of chemical reactions can be carried out using these approaches, which possess a number of attractive features for various molecular systems, such as proton transfer requiring a quantum mechanical treatment.

The quantum dynamical approach using wavepackets intrinsically tends to be complicated and imbalanced because the least and most appropriate wavefunctions corresponding to the RS and PS wavepackets are required to calculate the time-correlation functions.

In the diabatic picture, the Hamiltonian is divided into nonreactive (reactant and product) and reactive parts. In particular, the reaction probability is evaluated in terms of the transition between two nonreactive surfaces. The wavefunctions corresponding to the RS and PS, which are necessary to calculate the time-correlation functions, can be easily obtained in the diabatic picture. Therefore, to employ a simple potential construction and quantum dynamics simulation using the diabatic picture for the quantum mechanical rate constant is important for analyzing proton transfer reactions, including large molecular systems [76], based on a quantum mechanical treatment.

In this chapter, a simple method for thermal rate constant of intermolecular proton transfer reactions using quantum dynamics simulations on the constructed diabatic potential is proposed. The diabatic potential construction is performed referring to the

previous chapter. This chapter is focused on the (a) $WatH^+$-Wat and (b) AmH^+-Am pairs as homo-molecular proton transfer systems, and on the (c) AmH^+-Wat pairs as hetero-molecular systems, the structures of which are shown in Fig. 4.1. The validity of proposed the method is then demonstrated for these proton transfer systems.

4.2 Theoretical methods

4.2.1 Adiabatic and Diabatic representations

In this section, the adiabatic and diabatic representations used for PES construction and the quantum dynamics simulation are explained. An outline of the formalism of these representations is given in chapter 2. Here, the important equations in this chapter are shown.

In the adiabatic and diabatic representations, for two-state system, the nuclear wavefunction $\{\chi_n\}$ satisfies the following equation:

$$i\hbar\frac{\partial}{\partial t}\begin{pmatrix}\chi_1^{\rm ad}\\ \\ \chi_2^{\rm ad}\end{pmatrix}=\begin{pmatrix}T_1 & \Lambda_{12}\\ \\ \Lambda_{21} & T_2\end{pmatrix}\begin{pmatrix}\chi_1^{\rm ad}\\ \\ \chi_2^{\rm ad}\end{pmatrix}+\begin{pmatrix}\epsilon_1 & 0\\ \\ 0 & \epsilon_2\end{pmatrix}\begin{pmatrix}\chi_1^{\rm ad}\\ \\ \chi_2^{\rm ad}\end{pmatrix}, \tag{4.1}$$

$$i\hbar\frac{\partial}{\partial t}\begin{pmatrix}\chi_1^{\rm di}\\ \\ \chi_2^{\rm di}\end{pmatrix}=\begin{pmatrix}T_1 & 0\\ \\ 0 & T_2\end{pmatrix}\begin{pmatrix}\chi_1^{\rm di}\\ \\ \chi_2^{\rm di}\end{pmatrix}+\begin{pmatrix}V_{11}^{\rm di} & V_{12}^{\rm di}\\ \\ V_{21}^{\rm di} & V_{22}^{\rm di}\end{pmatrix}\begin{pmatrix}\chi_1^{\rm di}\\ \\ \chi_2^{\rm di}\end{pmatrix}. \tag{4.2}$$

In the adiabatic representation, the adiabatic potential $\boldsymbol{V}^{\mathrm{ad}}$ is diagonal, while the kinetic energy operator $\boldsymbol{T}^{\mathrm{ad}}$ includes the non-adiabatic coupling matrix. On the other hand, in the diabatic representation, the kinetic energy operator $\boldsymbol{T}^{\mathrm{di}}$ is diagonal, but the potential energy operator $\boldsymbol{V}^{\mathrm{di}}$ contains off-diagonal matrix elements, where V_{11}^{di} and V_{22}^{di} are diabatic potentials; V_{12}^{di} and V_{21}^{di} are non-diagonal matrix elements.

4.2.2 Quantum dynamics simulation

In this section, the reactive scatting theory using quantum dynamics simulation is explained. An outline of the theory is also given in chapter 2. Here, the important formulations are shown. We consider the two general wave packets that correspond to the RS and PS: the incoming $|\phi_\alpha\rangle$ and outgoing $|\phi_\beta\rangle$ wavepackets. According to the Eq. (2.81), using the Fourier transform of the time-correlation function, a time-dependent reactive scattering formula is equivalent to the following:

$$|S_{\beta,\alpha}(E)|^2 = \frac{|\int_{-\infty}^{\infty}\langle\phi_\beta|e^{-iHt/\hbar}|\phi_\alpha\rangle e^{iEt/\hbar}dt|^2}{|\int_{-\infty}^{\infty}\langle\phi_\alpha|e^{-iHt/\hbar}|\phi_\alpha\rangle e^{iEt/\hbar}dt||\int_{-\infty}^{\infty}\langle\phi_\beta|e^{-iHt/\hbar}|\phi_\beta\rangle e^{iEt/\hbar}dt|}. \tag{4.3}$$

However, to compute the state-to-state matrix elements, the incoming and outgoing wavepackets corresponding to the RS and PS need to be obtained. In addition, while these wave packets are obtained using the Møller operator, the Hamiltonian must be

divided into an asymptotic part and an interaction potential that goes to zero asymptotically in the adiabatic picture.

On the other hand, in the diabatic picture, if diabatic potentials V_{11}^{di} and V_{22}^{di} are obtained, the reactant and products states can be easily separated. In a diabatic representation, according to Eq. (4.2), the time correlation function of the reaction can be written as

$$\langle \phi_\beta | e^{-iHt} | \phi_\alpha \rangle = \int dr \chi_\beta^*(r) \exp(-iV_{12}^{\mathrm{di}}(r)t) \chi_\alpha(r) \tag{4.4}$$

using the eigenfunction $\chi_{\alpha,\beta}$ of diabatic potentials V_{11}^{di} and V_{22}^{di}. The S-matrix is then obtained by the Fourier transform of the time correlation function.

In this work, the one-dimensional diabatic potentials V_{11}^{di} and V_{22}^{di}, and V_{12}^{di} for proton transfer were first constructed. According to Eq. (4.4), the time correlation function is then calculated using the V_{12}^{di} and the eigenfunction of obtained the V_{11}^{di} and V_{22}^{di} potentials as $\chi_{\alpha,\beta}$. The analytical function as $\chi_{\alpha,\beta}$ using eigenfunction of Morse potentials as V_{11}^{di} and V_{22}^{di} was utilized. Finally, S-matrix was calculated by the Fourier transform obtained the time correlation function.

According to chapter 2, $|S_{\alpha,\beta}(E)|^2$ corresponds to the reaction probability from the RS (α) to PS (β) denoted by $P_{\alpha\beta}$. Using the reaction probability, the thermal rate constant for proton transfer systems was estimated. In this work, the state selected

total reaction probability with the ground state as the reactant state, $\sum_\beta P_{0\beta}(E)$ was used. Thus, the rate constant can be written as

$$k^{\mathrm{QD}}(T) = \frac{1}{h}\frac{1}{Q}\sum_{\beta}\int_0^\infty \exp\left(-\frac{E}{kT}\right) P_{0\beta}(E)dE, \tag{4.5}$$

where Q is the reactant partition function.

In this study, for one-dimensional intermolecular proton transfer, the proton transfer rate constant was estimated using Eq. (4.5). $P_{0\beta}$ based on the set of squares of the obtained S-matrix using the ground state of V_{11}^{di} and the eigenfunctions set of V_{22}^{di}. Transition state theory (TST) is widely used to estimate rate constants for proton transfer systems if transition states (TS) are found. In TST, rate constants can be estimated from the free energies for the optimized RS and TS geometries. In this work, to compare with the TST, the proton transfer rate constant was estimated using TST for (b) AmH^+-Am as an example of having a TS.

4.2.3 Calculation model

In the construction of the PES for proton transfer, we began by focusing on three proton transfer models: (a) $WatH^+$-Wat and (b) AmH^+-Am as homo-molecular pairs and (c) AmH^+-Wat as a hereto-molecular pair, as shown in Fig. 4.1. Figure 4.2 also shows

these models and PES coordinates. For homo-molecular pairs, coordinate R denotes the intermolecular distance and x is the translating proton position, which is defined as the displacement from the center of the intermolecular distance. For a hetero-molecular pair, r is used as the displacement between a proton-bonded atom and the proton.

4.2.4 Diabatic potential functions (V_{11}^{di}, V_{22}^{di}) and optimization of potential parameters

In this chapter, a PES for proton transfer was constructed using the diabatic picture. The PES was constructed using the Morse potentials as V_{11}^{di} and V_{22}^{di} functions. The explicit functional forms were defined in the previous chapter, i.e., Eqs. (3.6)-(3.8) and (3.9)-(3.11). The detailed optimization procedure of the potential parameters in V_{11}^{di} and V_{22}^{di} was also shown in the previous chapter. Although the Morse potential as V_{11}^{di} and V_{22}^{di} was used to construct the PES, the Gaussian function as non-diagonal matrix element V_{12}^{di}, which was utilized in the previous chapter, was not used in this chapter. Here, to construct the exact PES, polynomial function was used as V_{12}^{di}.

4.2.5 Adiabatic potential energy calculation

To obtain the one-dimensional adiabatic PES $V^{\mathrm{ad}}(x;R)$ or $V^{\mathrm{ad}}(r;R)$ for the proton-transfer reaction, quantum chemical calculations were performed with stepwise move-

ment of the proton by 0.02 Å. The geometries of the molecules, except for the proton position and the intermolecular distance, were then kept as the minimum energy structures. The minimum energy structures, as shown in Fig. 4.1, were determined by geometrical optimization. The adiabatic potential energies were calculated by moving the proton position for a fixed intermolecular distance. The following intermolecular distances were then used: 2.39 Å for (a) $WatH^+$-Wat, 2.69 Å for (b) AmH^+-Am, and 3.03 Å for (c) AmH^+-Wat. Finally, the adiabatic potential energies were fitted using a polynomial series function of the fourth order with respect to x or r. All DFT calculations were performed the CAM-B3LYP/aug-cc-pVTZ level using the Gaussian-09 package [56].

4.3 Results and Discussion

4.3.1 Construction of diabatic potential

After construction of the diagonal part of the potentials as $V_{11}^{\rm di}$ and $V_{22}^{\rm di}$ for (a) $WatH^+$-Wat, (b) AmH^+-Am, and (c) AmH^+-Wat, we turned our efforts to estimating the non-diagonal part as $V_{12}^{\rm di}$. Using $V_{11}^{\rm di}$, $V_{22}^{\rm di}$, and $V^{\rm ad}$ obtained by the DFT calculations,

we estimated the defined values of V_{12}^{di} based on Eq. (3.2) using the following equation:

$$V_{12}^{\mathrm{di}} = \sqrt{\left(\frac{V_{11}^{\mathrm{di}} + V_{22}^{\mathrm{di}}}{2} - V^{\mathrm{ad}}\right)^2 - \left(\frac{V_{11}^{\mathrm{di}} - V_{22}^{\mathrm{di}}}{2}\right)^2}. \tag{4.6}$$

Figure 4.3 shows the computed V_{11}^{di} and V_{22}^{di} and possible V_{12}^{di} values with V^{ad} for (a) WatH^+-Wat, (b) AmH^+-Am, and (c) AmH^+-Wat. For all pairs, V_{11}^{di} and V_{22}^{di} reproduce the adiabatic potential at the location where the proton position is closer to a binding atom than a stable point ($r < r_0$). For homo-molecular pairs, V_{12}^{di} shows similar symmetrical behavior with respect to $x = 0$, which has its maximum value at the crossing point of V_{11}^{di} and V_{22}^{di}. On the other hand, for a hetero-molecular pair, the V_{12}^{di} exhibits asymmetrical behavior with respect to the crossing point of V_{11}^{di} and V_{22}^{di}, while the maximum value of V_{12}^{di} is located at the crossing point of V_{11}^{di} and V_{22}^{di} and shows the same behavior for homo-molecular pairs.

Therefore, a PES for various proton transfer systems can be reproduced using V_{11}^{di} and V_{22}^{di} with the Morse potential to describe the vibrational motion, and V_{12}^{di} with the maximum value at the crossing point of V_{11}^{di} and V_{22}^{di}. Eq. (4.6) shows that the value of V^{ad} is lower for larger values of V_{12}^{di}. Thus, V_{12}^{di} contributes to the stability of the adiabatic potential. In addition, according to the VB picture, V_{12}^{di} generally corresponds to the mixture or interaction between the two VB states, which contributes to the

possibility of proton transfer. Figure 4.3 shows that the ratio of the contribution to the stability of the potential and the possibility of proton transfer is the largest at the crossing point of V_{11}^{di} and V_{22}^{di} for all proton transfer systems. For (c) AmH^+-Wat, the V_{12}^{di} values over the water molecule side region ($r > r_c$) are larger than the ones over the ammonia molecule side region ($r < r_c$). This result indicates that proton transfer occurs easily over the water molecule side region ($r > r_c$).

In this work, the shape of the V_{12}^{di} curve obtained from Eq. (4.6) showed a different behavior than the Gaussian function when the conventional EVB approach was utilized, and it should be especially noted that the Gaussian function did not reproduce the asymmetrical shape of V_{12}^{di} for AmH^+-Wat. Therefore, in this chapter to construct the exact PES, the V_{12}^{di} values were fitted using a sixth-order polynomial series with respect to x for homo-molecular pairs, and a fifth-order polynomial series with respect to r for a hetero-molecular pair. Figure 4.4 shows the transformed adiabatic potentials obtained using Eq. (3.2) as V_{12}^{di}, which were derived from the diabatic potentials obtained from polynomial and Gaussian functions, along with the adiabatic potentials from DFT for (c) AmH^+-Wat. The figure shows that the transformed adiabatic potential using the Gaussian function as V_{12}^{di} does not explicitly reproduce the one calculated using DFT over a region with a potential barrier.

4.3.2 Quantum dynamics simulation

Next, a quantum dynamics simulation was performed using obtained the diabatic matrix elements. Table 4.2 shows the rate constant and correlation time of proton transfer using quantum dynamics obtained from Eq. (4.5) at 298 K. For (b) AmH^+-Am, the rate constant obtained using TST, which is also listed in the table, was good agreement with the one obtained using quantum dynamics. Previously, the quantum dynamics simulation was carried out for (a) $WatH^+$-Wat in order to calculate the vibrational frequency [79], while Born-Oppenheimer molecular dynamics simulation was carried out for (c) AmH^+-Wat [80]. Table 4.2 lists the results for reference purposes, which were also in good agreement with the values in previous works. Thus, the validity of our method using diabatic potentials was confirmed.

In this study, we focused on the proton transfer system, which required the use of the quantum dynamics approach in order to treat the quantum effects, and proposed a simple quantum dynamics approach for the system using diabatic potentials. Using this approach, the computational costs can be reduced, and the simulation can be stably implemented. For example, the conventional split-operator method requires a large number of Fourier transforms, which is more than one million in this case, while our approach requires less than fifty Fourier transforms. Additionally, since the eigenfunctions of the Morse potential were used for the wavefunctions and, using Eq. (4.4),

were used to carry out the quantum dynamics simulation, wavefunction collapse was prevented.

Our quantum dynamics approach can be applied to the EVB potential, which has been used to carry out classical molecular dynamics, because the approach is based on the diabatic potential. Additionally, in contrast to TST, this approach can be used to estimate the proton transfer rate constant, even when it is difficult or impossible to search for a TS, such as when a large-scale system is used, or when no TS exists.

4.4 Conclusion

In this chapter, a simple method for thermal rate constant of intermolecular proton transfer reactions using quantum dynamics simulations on the constructed diabatic potential was proposed. For all homo- and hetero-molecular pairs, the potentials determined using a Morse potential as V_{11}^{di} and V_{22}^{di} and polynomial function as V_{12}^{di} were in good agreement with the ones determined using DFT. The proton transfer rate constants determined by applying a quantum dynamics simulation to the diabatic potentials were also in good agreement with the reference values. In this approach, wavefunctions corresponding to the RS and PS were determined uniquely for the quantum dynamics simulation. Furthermore, since the construction of the PES and the quantum

dynamics simulation can be carried out easily for homo- and hetero-molecular pairs, this method can be applied to intermolecular proton transfer estimations for various large molecular systems such as proteins, even when it is impossible to search for the TS.

Table 4.1: Diabatic potential energy parameters for (a) $WatH^+$-Wat, (b) AmH^+-Am, and (c) AmH^+-Wat.

(a) $WatH^+$-Wat		(b) AmH^+-Am	
D(kJ mol^{-1})	r_0(Å)	D(kJ mol^{-1})	r_0(Å)
663.3	0.974	735.0	1.024
(c) AmH^+-Wat			
D_1(kJ mol^{-1})	D_2(kJ mol^{-1})	r_0(Å)	r_0'(Å)
735.0	663.3	1.024	0.974

Table 4.2: Proton transfer rate constants and correlation times using quantum dynamics at 298 K.

	(a) $WatH^+$-Wat	(b) AmH^+-Am	(c) AmH^+-Wat	
			Forward	Reverse
R value (Å)	2.39	2.69	3.03	
Rate constant (s^{-1})	5.56×10^{13}	1.26×10^{14}	4.64×10^{13}	7.97×10^{13}
Correlation time (fs)	18.0	7.94	21.6	12.5
Reference (s^{-1})	$3.0 - 6.0 \times 10^{13}$[*]	2.27×10^{14}[**]	$5.0 - 10.0 \times 10^{13}$[***]	

* The rate constant was obtained by converting the frequency determined in a previous work [79].

** The rate constant was obtained using transition state theory (TST).

*** The rate constant was obtained from Born-Oppenheimer molecular dynamics simulations [80].

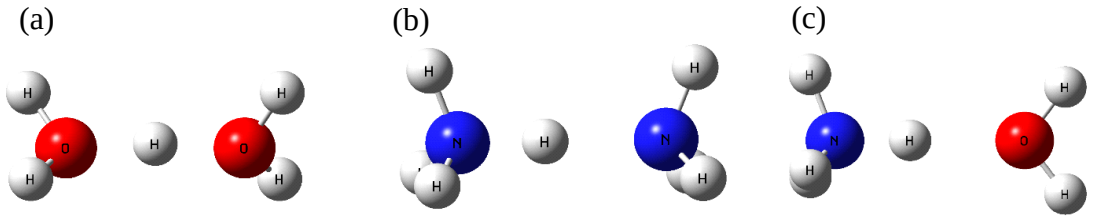

Figure 4.1: Stable structures of the proton-bonded (a) $WatH^+$-Wat, (b) AmH^+-Am, and (c) AmH^+-Wat pairs.

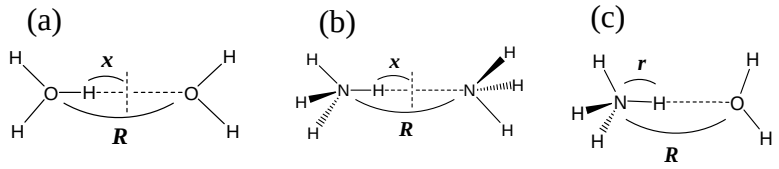

Figure 4.2: Proton transfer model and potential energy coordinates for (a) $WatH^+$-Wat, (b) AmH^+-Am, and (c) AmH^+-Wat.

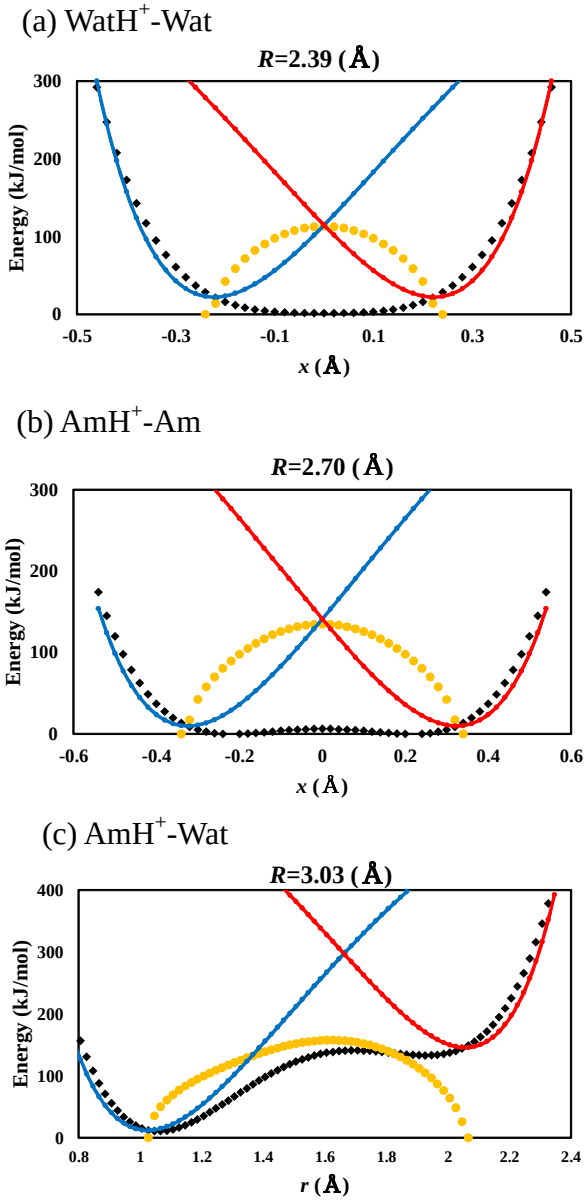

Figure 4.3: Diabatic potentials V_{11}^{di} (blue line) and V_{22}^{di} (red line) computed using obtained parameters, and adiabatic potential from DFT calculations (black dots), and the possible V_{12}^{di} values (yellow dots) estimated based on the Eq. (4.6) for (a) $WatH^+$-Wat, (b) AmH^+-Am, and (c) AmH^+-Wat.

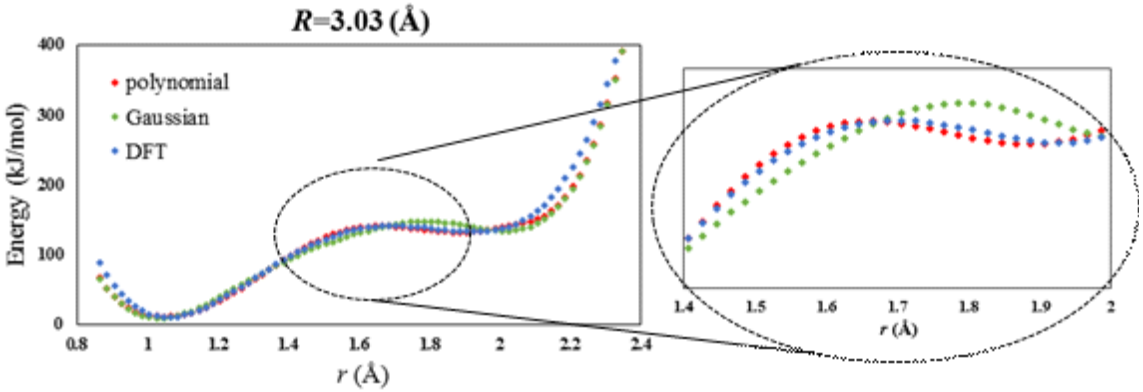

Figure 4.4: Transformed adiabatic potential using Eq. (3.2) derived from the diabatic potentials obtained from polynomial (red dots) and Gaussian functions (green dots) and from DFT (blue dots) for AmH^+-Wat.

Chapter 5

Application to Intermolecular Proton Transfer using Diabatic Potential in Proton Conductive Material

In chapters 3 and 4, we discussed the construction of potential energy surface (PES) using diabatic picture and quantum rate constants using quantum dynamics simulation on the PES for intermolecular proton transfer. In this chapter, this approach is applied to intermolecular proton transfer in proton conductive material as an example of a large molecular system. In addition, the proton conductive path is discussed in terms of intermolecular proton transfer. In the following, the specific introduction of this chapter is explained in section 1; theoretical and computational methods are explained in section 2; results and discussion are explained in section 3; and finally conclusion is

explained in section 4.

5.1 Introduction

Anhydrous proton-conductive materials can be utilized as solid electrolytes in fuel cells and have been widely developed for their applications due to stability above 100 ℃. Especially, composite materials of strong acids polymers and basic molecules such as imidazole and its derivatives have been considered to be polymer electrolytes under anhydrous conditions and has been proposed [84–95]. For instance, poly(vinylphosphonic acid) (PVPA)-imidazole (Im) (PVPA-xIm) [86,88] and alginic acid (AA)-Im (AA-xIm) composite materials [87], where x represents the number of moles of Im per mole of polymer repeat unit, are examples of the composite materials, of which proton conductivity increase with increasing x. The proton conductivities of PVPA-xIm and AA-xIm have maximum values of 7×10^{-3} at 150 ℃ for $x = 8$ [88] and 2×10^{-3} S/cm at 130 ℃ for $x = 2$ [87], respectively. PVPA-xIm includes a strong phoshonic acid polymer with the high proton-exchange capacity, while AA-xIm is non-toxic and low cost biopolymer formed from mannuronic and guluronic monomers with a carboxylic group. For these materials, Im molecules are intercalated into host polymers PVPA and AA, while these polymers function as source of excess protons and encourage the proton conduction.

To develop the high proton-conductive materials, it is important to understand the proton conductive mechanism in these materials. The widely recognized mechanism is the proton transport in the materials involving structural diffusion known as the Grotthuss-type mechanism [96]. In the Grotthuss-type mechanism, intermolecular proton transfer occurs followed by reorganization of hydrogen bond. The rate limiting step then involves a molecular motion of breaking of short, strong hydrogen bonds such as rotation of imidazole molecule.

In the previous works, for a system of only Im molecules, a number of researches for microscopic proton conductive mechanism have been conducted using various techniques such as solid-state NMR [97, 98], molecular dynamics simulation [24, 27, 81, 99, 100], and quantum chemical calculation [20, 83]. For example, Münch and coworkers [81] reported that the presence of an excess proton results in local disorder in a system of imidazole chains, and proton transfer along the hydrogen bonding in imidazole is 2 orders of magnitude faster than the reorientation of imidazole by using Car-Parrinello molecular dynamics (CPMD) simulations. Their results emphasize that the reorientation of imidazole is a limiting step of proton conduction. Voth and co-workers [24] performed a multi empirical valence bond (MS-EVB) method to estimate a proton diffusion coefficient and Grotthuss hopping rate and investigate the relationship between proton transport and structures of solvation shell of imidazolium

cation. In construct, solid-state NMR was also measured to investigate the relationship between proton conductivity and molecular motion by considered proton conductivity as proton diffusion [97]. Furthermore Kumar and Venkatnathan [83] characterized the proton transport and rotation energy barriers in a system of imidazole chains by density functional theory. They showed that the presence of the proton had stronger effect on the immediate neighboring imidazole molecules, and the effect was negligible after two molecules. They also found that the rotational barrier was higher than the proton transport barrier along the hydrogen bond and the rate determining step of proton conduction. Therefore the formation and cleavage of hydrogen bonds between imidazole molecules play a key role in proton conduction by molecular motion of imidazole like rotation in liquid or crystal of only imidazole, which is the rate limitting step of proton conduction.

On the other hand, there have been proposed some proton-conductive materials in the crystalline solid [77, 78]. Imidazolium hydrogen succinate (Im-Suc) crystals can be utilized as solid electrolytes and have gained considerable attention. The proton conductivity increased from 1×10^{-5} to 1×10^{-3} S/cm in a temperature range of 330-400 K in the fact of crystalline solid of the material [78]. Such proton conductivity results from continuous proton transfer between the imidazolium ions and the carboxyl groups in the hydrogen network and the reorientational motion of the imidazolium ions based

on the Grotthuss-type mechanism [81–83]. Figure 5.1 shows the projection of a single layer parallel to the (01-1) plane obtained by X-ray diffraction measurements. [77, 78] The distance between the layers is 3.385 Å. The proton diffusion path was along the [100] direction or along the [14-9] direction and includes the proton transfer process between imidazole and succinic acid and between succinic acid and succinic acid. In the previous work [82], the dynamics of imidazolium ions for Im-Suc was investigated using solid-state ^{2}H and ^{13}C NMR. These measurements indicated that imidazolium ion libration played an important role in the proton conductive process. However, there has been little in the way of investigation into the local proton transfer process used by Im-Suc even though proton transfer certainly occurs during the proton conductive process.

In an analysis of proton transfer for large-scale system such as Im-Suc, transition state theory (TST) generally cannot be used to estimate the proton transfer rate constants, because it is difficult or impossible to search for TS. Therefore, in this chapter, to estimate the rate constant of intermolecular proton transfer for Im-Suc, diabatic potentials construction and quantum dynamics simulation on the potentials are performed using the approach discussed in chapters 3 and 4. In addition, the proton conductive path is discussed in terms of intermolecular proton transfer.

5.2 Theoretical and computational methods

Figure 5.1 shows the projection of the single layer parallel to the (01-1) plane obtained by X-ray diffraction measurement [77, 78] for Im-Suc. The distance between the layers is 3.385 A. The proton diffusion path was along the [100] direction or along the [14-9] direction and includes the proton transfer process between imidazole and succinic acid (N...O) and between succinic acid and succinic acid (O...O). In this chapter, we focus on three layers (a single layer is shown in Fig. 5.1) as a model of the material and performed processing using "our own n-layered integrated molecular orbital and molecular mechanics" (ONIOM) approach. The potential energies and proton transfer rate constant for between imidazole and succinic acid (N...O) and between succinic acid and succinic acid (O...O) in the middle layer of three layers were calculated. Furthermore, to add the influence of the other two up-and-down layers, which interact electronically with the middle layer, the other two layers except for the middle layer were also calculated. The high-level region has one imidazole and two succinic acids related to concerted proton transfer, as shown in Fig. 5.2 (ball and stick model), while the other molecules correspond to the low-level region. The high- and low-level regions were calculated at the CAM-B3LYP/aug-cc-pVDZ and AM1 levels, respectively. Geometrical optimization was performed using the initial structure obtained by X-ray diffraction [78], and the structures were maintained with the exception of the proton

positions in the high-level region. To estimate the proton transfer rate constant for between imidazole and succinic acid (N...O) and between succinic acid and succinic acid (O...O), diabatic potentials construction and quantum dynamics simulation on the potentials were performed using the approach discussed in chapters 3 and 4. The detailed procedures of potential construction and rate constant estimation were utilized the ones discussed in chapters 3 and 4. In the PES construction using diabatic picture, Morse potential was used as V_{11}^{di} and V_{22}^{di}, while a fifth-order polynomial series was used as V_{12}^{di}.

5.3 Results and Discussion

Table 5.1 shows the lengths of the hydrogen bonds and intermolecular distances (Å) for the concerting proton transfers. The table shows that a proton between the imidazole and succinic acid is bonded to the imidazole molecule instead of O2 and the proton between the succinic acids is bonded to O1. This result indicates that the stable structure for Im-Suc is the charge-separated state corresponding to the imidazolium cation and the succinic anion. This result is in agreement with previous works on probability density function analysis using X-ray diffraction.

The diabatic potential for proton transfer and estimated its rate constant were

then constructed. Figure 5.3 shows the transformed adiabatic potential derived from the obtained diabatic potentials using Eq. (3.2) for N→O and O1→O2. This result indicates that proton transfer PES for large-scale system such as Im-Suc, even when there is no TS, can be reproduced using V_{11}^{di} and V_{22}^{di} with Morse potential described the vibrational motion and V_{12}^{di} with the polynomial function.

Table 5.2 also shows the obtained rate constant results. Because the corresponding correlation times are approximately $4 - 20$ fs for all proton transfer systems, proton transfer is faster than the molecular motion of imidazole in Im-Suc crystals. Comparing the rate constants of the proton transfers between imidazole and succinic acid (N...O) and between succinic acid and succinic acid (O...O), we find that the rate constant for N→O, k(N→O), is larger than that for O1→O2, k(O1→O2). The rate constant ratio of the proton transfer k(N→O)/k(O1→O2) was 1.50, which indicates that the N→O proton transfer was one-and-a-half times as large as that of O1→O2.

From the stable structures, we find that the proton is bonded to imidazole in Im-Suc. If the proton diffusion process contributes to the proton conductive mechanism, imidazole plays the role of carrier for proton conduction. In a previous work, it was suggested that the conductive path for continuous proton transfer was in the hydrogen network of the (01-1) plane, and an analysis of the anharmonic probability density functions [78] indicated that the potential barriers to proton diffusion along the [100]

axis were lower than those along the [14-9] axis. The two results suggested the direction of the proton diffusion path, as shown in Fig. 5.1. In the previous work [78], it was shown that the proton diffusion path along the [100] direction occurred only through proton transfer between N...O, while that along the [14-9] direction occurred via proton transfer between both N...O and O...O. Therefore, the proton diffusion path along the [100] direction occurs more easily than along the [14-9] direction. The rate constant results from Table 5.2 show that the proton transfer between O...O is more difficult than that between N...O. This result is consistent with the suggested proton diffusion path.

In the previous work [82], the dynamics of imidazolium ions for Im-Suc was investigated using solid-state ^{2}H and ^{13}C NMR. These measurements indicated that imidazolium ion libration played an important role in the proton conductive process. Therefore, we can conclude that the proton conductivity in Im-Suc crystal results from the continuous proton transfer between N...O in the hydrogen network with [100] direction and the imidazole ion libration based on the Grotthuss-type mechanism.

In this chapter, it was confirmed that it was possible to construct the PES for proton transfer using a diabatic picture for large molecular systems. In addition, a rigorous rate constant using a quantum dynamics simulation was estimated for Im-Suc. This approach can facilitate simple proton transfer estimations for various large molecular

systems, and it is possible that this approach can be applied to biomolecular systems.

5.4 Conclusion

To develop the high proton-conductive materials, it is important to understand the proton conductive mechanism. The proton conductivity for Im-Suc crystal results from continuous proton transfer between the imidazolium ions and the carboxyl group in the hydrogen network and the reorientational motion of the imidazolium ions. The proton diffusion path was along the [100] direction or along the [14-9] direction and includes the proton transfer process between imidazole and succinic acid and between succinic acid and succinic acid. In this chapter, to estimate the rate constant of intermolecular proton transfer for Im-Suc, diabatic potentials construction and quantum dynamics simulation on the potentials were performed using the method discussed in chapters 3 and 4. The results indicated that the proton transfer rate constant of N→O was one-and-a-half times as large as that of O1→O2. Furthermore, in the Im-Suc crystal, it was found that in terms of local proton transfer, proton diffusion with proton transfer occurred more easily along the [100] axis than along the [14-9] axis.

Considering the results using solid-state NMR in the previous work, we conclude that the proton conductivity in Im-Suc crystal results from the continuous proton transfer

between N...O in the hydrogen network with [100] direction and the imidazole ion libration based on the Grotthuss-type mechanism.

Table 5.1: Lengths of hydrogen bonds and intermolecular distances (Å) for concerting proton transfer for Im-Suc. Atomic labels are shown in Fig. 5.2.

N…O2	2.72
N−H	1.04
O1…O2	2.48
O1−H	1.06

Table 5.2: Proton transfer rate constants between nitrogen and oxygen (N…O), and oxygen and oxygen (O…O) using quantum dynamics at 298 K for Im-Suc. Atomic labels are shown in Fig. 5.2.

	N…O		O…O	
Direction of proton transfer	N→O2	O2→N	O1→O2	O2→O1
Rate constant (s^{-1})	9.88×10^{13}	2.24×10^{14}	6.60×10^{13}	1.88×10^{14}
Correlation time (fs)	10.13	4.46	15.14	5.33

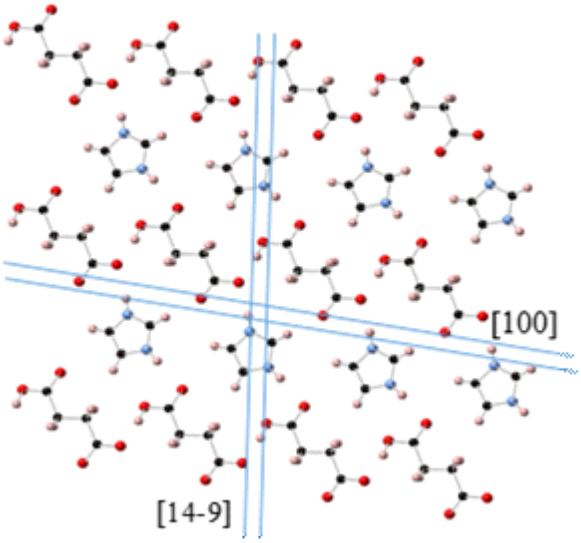

Figure 5.1: Projection of the single layer parallel to the (01-1) plane for Im-Suc, and illustration of the suggested proton paths in the layer [78].

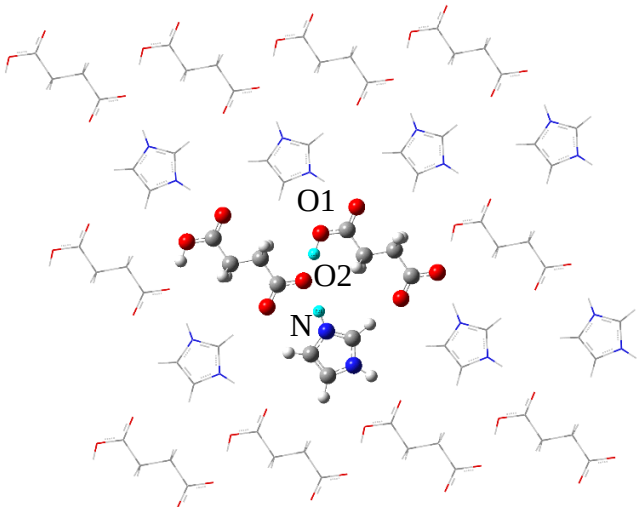

Figure 5.2: The partition of high and low level areas is shown for ONIOM calculations. The high-level area model is shown as the ball and stick model in the middle of three layers. The low-level area model is the other region. The concerting protons are aqua, and the nitrogen and oxygen atoms are labeled with atom numbers.

(a) N→O

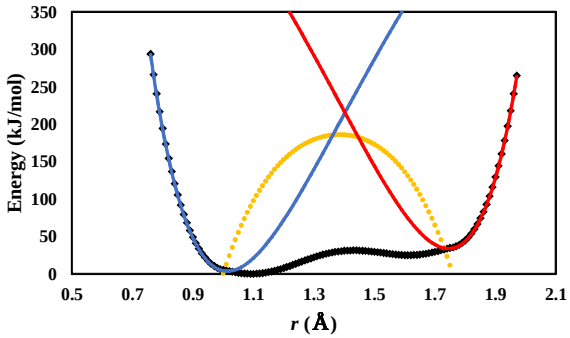

(b) O1→O2

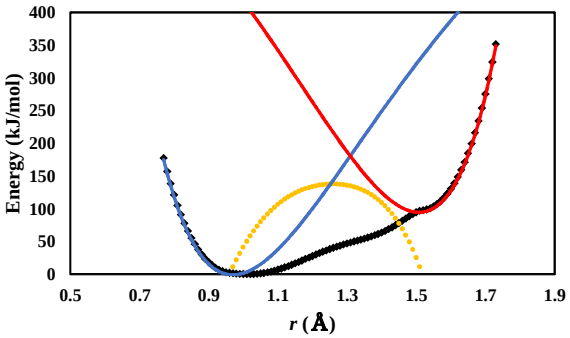

Figure 5.3: Transformed adiabatic potential derived from the diabatic potentials using Eq. (3.2) (black dots), diabatic potentials V_{11}^{di} (blue line) and V_{22}^{di} (red line), and the V_{12}^{di} values (yellow dots) for (a) N→O and (b) O1→O2.

Chapter 6

Application to Analysis of Reaction Involving a Proton using the Adiabatic Potentials

In this chapter an analysis of the reaction involving proton using adiabatic potentials instead of diabatic potentials is discussed. This chapter is investigated the hydride transfer process including a proton and intrinsic reaction coordinate (IRC) as adiabatic potential. Using the IRC, the details of change in geometries, solvent effect, and charge transfer process can be investigated. This chapter is focused on a hydride transfer system in which formaldehyde (CH_2O) acts as the hydride acceptor and lithium aluminum hydride ($LiAlH_4$) or lithium borohydride ($LiBH_4$) acts as the hydride donor. In the following, the specific introduction of this chapter is explained in section 1; computational details are explained in section 2; results and discussion are explained in section 3; and

finally conclusion of this chapter is explained in section 4.

6.1 Introduction

Reductions involving hydride transfers are some of the most important chemical reactions in biochemistry and organic chemistry [101–103]. As an example, NADPH [104], $FADH_2$ [105], tetrahydrofolate [106] and ascorbic acid [107], all of which play vital roles in biological redox systems, are naturally-produced organic hydride donors. The reductions of ketones [108], aldehydes [109], alkenes [110], alkyl halides [111] and imines [112] are also well-known reactions involving hydride transfers. As such, there is considerable interest among researchers regarding the design and synthesis of new organic compounds via hydride reductions.

Hydride transfer is a key process in hydride reduction and so, to elucidate the associated reaction mechanism, it is important to understand the hydride reduction mechanism. In previous works, the hydride transfer mechanisms in many biological and organic reduction systems were investigated using either experimental or theoretical approaches [113–124]. Although these mechanisms have not yet been fully explained due to the variety of possible pathways involving the overall transfer of two electrons and one proton, the following hydride transfer mechanisms have been proposed: (1)

direct transfer of a hydride ion (H^-) in a single step, (2) two-step transfer of an electron before or after the transfer of a hydrogen atom and (3) transfer of two electrons and one proton in three separate steps. Several experimental studies have provided evidence for the single-step mechanism [125–128], although the multi-step mechanism has also been suggested [119, 128, 129]. Therefore, although the hydride transfer mechanism has been researched over a significant time period, there is little agreement as to the detailed reaction steps.

Theoretical studies aimed at understanding the hydride transfer mechanism have also been conducted, focusing on the effects of the charge density, ionization potential and proton affinity of the reactant and transition state [113–118,121,123,124]. However, as far as we know, there are no reports of detailed charge density analysis along the reaction coordinates during hydride transfer, although it requires complete information regarding the dynamics of the mechanism. Furthermore, hydride transfer process would be strongly affected by various solvent species, because the process involves the transfer of two electrons and it is well known that the dynamics and kinetics of such transfers are affected by the solvent.

In the present chapter, we focused on a hydride transfer system in which CH_2O acts as the hydride acceptor and $LiAlH_4$ or $LiBH_4$ acts as the hydride donor. $LiAlH_4$ and $LiBH_4$ have both been widely used in organic syntheses as reducing agents, although

$LiAlH_4$ is more powerful than $LiBH_4$ owing to the weaker Al-H bond compared to the B-H bond [103]. A suggested hydride reduction mechanism using these reducing agents is shown in Fig. 6.1. The reaction path, geometries and energies of the complexes and transition state (TS) structures in these reactions have been previously investigated using many experimental and theoretical approaches [130–139]. These studies have identified the importance of the association of the lithium cation with the carbonyl oxygen during reduction by $LiAlH_4$ or $LiBH_4$. In addition, it was found that this structures remained in solvent by Car-Prrinello molecular dynamics simulations about a solution of $NaBH_4$ in liquid methanol [139]. Both carbonyl carbon-14 and deuterium isotope studies during the reduction of benzophenone with $NaBH_4$, $LiBH_4$ and $LiAlH_4$ have shown that changing the metal atom from Al to B shifts the transition state geometry from reactant-like to central, and that varying the solvent can generate a product-like TS [139]. Furthermore it is necessary to study the behavior of hydrides in terms of their geometries, energies and charge densities to fully understand the hydride transfer mechanism. Tetrahydrofuran (THF) is often used as the solvent during laboratory-scale hydride reduction with $LiAlH_4$ and $LiBH_4$. Therefore, we also study the behavior of hydrides for polarizability of THF.

In this work, we calculated optimized geometries for the reactant, transition and product states both under vacuum and in THF, focusing on changes in the dynamics of

transferring the H atom as well as the charge density along the reaction coordinate. The reduction of CH_2O using either $LiAlH_4$ or $LiBH_4$ was assessed. To accomplish this, we calculated IRC both under vacuum and in THF for these reaction systems, and analyzed the molecular and electronic structures along the IRC using density functional theory (DFT). Based on the results, we deduced the essential hydride transfer mechanism by clarifying the charge transfer behavior along the IRC. Herein we discuss the differences in the reaction process observed when employing either $LiAlH_4$ or $LiBH_4$ as reagents by comparing the two systems in terms of their geometries, energies and charge densities.

6.2 Computational details

In this section, the computational details to calculate the hydride transfer are shown. All DFT calculations were conducted at the CAM-B3LYP/Aug-cc-pVTZ level with the Gaussian 09 software package [56]. The hydride transfer TS was optimized based on the results of previous studies [132, 138]. In addition, we calculated the energy of RS, TS, and PS using CCSD(T)/Aug-cc-pVTZ level for obtained above geometries to confirm the accuracy of CAM-B3LYP calculations. The polarizability of THF as the solvent effects was considered. The solvent effects were evaluated using the self-consistent reaction field polarizable continuum model (SCRF/PCM) [43, 140]. In previous work,

the solvation free energies and dipole moments of organic molecules obtained using SCRF/PCM were found to be in good agreement with experimental data [43]. To investigate the hydride transfer process in detail, we estimated the rearrangement parameter (α) and charge density of the fragments involved in the hydride transfer process along the IRC. Here α denotes the extent of transfer of a H atom from the reactant to product structures, and is defined as:

$$\alpha \equiv \frac{\Delta R_{\mathrm{X-H}}}{\Delta R_{\mathrm{C-H}} + \Delta R_{\mathrm{X-H}}} \qquad (\mathrm{X} = \mathrm{Al}, \mathrm{B}), \tag{6.1}$$

where $\Delta R_{\mathrm{C-H}}$ is obtained by subtracting the length of the bond between the carbon and the transferring H atom from the C-H bond length in the methoxide ion (CH_3O^-) and $\Delta R_{\mathrm{X-H}}$ is obtained by subtracting the length of the bond between the X atom and the transferring H atom from the X-H bond length in the XH_4^- reactant. A value of $\alpha = 0$ indicates that the structure at a given stage is close to the initial structure (that is, XH_4^-), while a value of $\alpha = 1$ corresponds to a structure more closely resembling that of the product (CH_3O^-). Charge density values were obtained by calculating the electrostatic potential fit (ESP) charges using the Merz-Killmann (MK) method. The charge distribution derived from ESP typically exhibits the best performance in both theoretical and experimental investigations [42,141,142], compared to data derived from

the Mulliken, Hirshfeld and Natural Population Analysis schemes [143], and is also used for the analysis of chemical trends [144].

6.3 Results and Discussion

To investigate the role of the lithium cation (Li^+) during hydride reduction by $LiAlH_4$ and $LiBH_4$, we first calculated the IRC for hydride transfers with and without Li^+. The activation energy (ΔE_a) and the energy difference (ΔE) between the reactant state (RS) and product state (PS) were then estimated, where ΔE_a and ΔE were obtained by subtracting the energy of the TS from the RS and the energy of the PS from the RS based on the IRC results, respectively. Table 6.1 summarizes the ΔE_a and ΔE values for hydride transfer under vacuum. To confirm the accuracy of CAM-B3LYP calculations, we also calculated the ΔE_a and ΔE values using CCSD(T) for obtained above geometries. The obtained ΔE_a and ΔE values were respectively 14.6 and -192 kJ/mol for $LiAlH_4$ system, while that values were 82.7 and -115 kJ/mol for $LiBH_4$ system, which were close agreement with the values using CAM-B3LYP (see Table 6.1). In the case of both reagents, these values indicate that ΔE_a is significantly decreased in the presence of Li^+, while ΔE is not greatly changed. These results are consistent with those of previous work [131]. These data suggest that the lithium cation

contributes to stabilization of the TS, and is an important factor promoting the hydride reduction.

Figure 6.2 shows the RS, TS and PS structures associated with hydride transfer via $LiAlH_4$ and $LiBH_4$-formaldehyde complexes under vacuum. The TSs were obtained by an optimization process, and the RS and PS were located along both sides of the IRC compared to the TS. The complex formation energies, obtained by subtracting the energies of formation of formaldehyde and $LiAlH_4$ or $LiBH_4$ from the RS energy, were determined to be -87.1 and -76.5 kJ/mol, respectively. These results indicate that formation of the complex (the RS), meaning the coordination of lithium to oxygen, occurs prior to transfer of the hydride to the carbonyl carbon [132]. With regard to the structures of the RS, TS and PS, no differences in bonding state were found between the $LiAlH_4$ and $LiBH_4$ complexes. In the RS and TS of both complexes, a lithium tridentate structure was identified, corresponding to the coordination of lithium to an oxygen and two hydrogens. The TS structures were found to be both six-centered cyclic forms, in which the $C\cdots H$ bond lengths generated when employing $LiAlH_4$ and $LiBH_4$ were 1.76 and 1.12 Å, respectively. Therefore the TS structure associated with $LiAlH_4$ reduction has a reactant-like geometry, whereas TS structure associated with $LiBH_4$ reduction is product-like. The PS obtained from both complexes has the same conformation, in which aluminum and boron are associated with oxygen, and the AlH_3 and BH_3

moieties are rotated to allow the coordination of lithium to one hydrogen, respectively. Furthermore, by comparing the ΔE_a and ΔE values for both complexes, we also found that the use of $LiAlH_4$ resulted in lower ΔE_a and ΔE compared to the results obtained with $LiBH_4$ [132, 138], in agreement with the experimental observation [139] that the reducing power of $LiBH_4$ is less than that of $LiAlH_4$.

To examine the solvent effects on the hydride transfer, we perform IRC calculation including one explicit molecule of THF and under PCM for $LiAlH_4$ system as the same method under Vacuum. Since THF is well-known to complex lithium, in explicit THF molecule, TS is explored based on the configurations in Vacuum and interacted THF to the lithium. Figures 6.3, 6.4(a) and table 6.2 show the structures of the RS, TS, PS, and relative energies (ΔE_a and ΔE) in explicit model and PCM for $LiAlH_4$ system. These results indicate that RS, TS, and PS structures have similar conformations for explicit model and PCM of THF. Also, relative energies are close values for these two models. In calculations of the explicit model with THF molecules, various geometries are expected to be obtained by the relative positions, orientations, and number of THF molecules. In this study, we focus on a local dynamics of hydride transfer, not the relationship between $LiAlH_4$ or $LiBH_4$ systems and explicit THF in detail. Therefore, the PCM calculation as the solvent effects was employed in following.

Table 6.3 shows the total energies of the RS, TS and PS as well as the ΔE_a and ΔE

values both under vacuum and in THF. In the case of both reagents, the total energies of the RS, TS and PS are all reduced when performing the reaction in THF, as are ΔE_a and ΔE. These results suggest that the TS and PS are more highly stabilized than the RS in the presence of THF.

Figure 6.4 presents the structures of the RS, TS and PS in THF. For both complexes, different TS structures were obtained with and without the solvent. When using $LiAlH_4$, the TS structure contains bidentate lithium, in which lithium is coordinated to an oxygen and a hydrogen, while a tridentate structure appears under vacuum. In contrast, for the $LiBH_4$ system, a linear structure with a Li-O-C bond was identified. It is evident that these structures involve more charge separation, and thus is more highly stabilized by the presence of a solvent, in agreement with the results of previous work [132, 136]. Especially, when using LiBH4, the solvent thus has a more significant effect on the activation energy compared with the $LiAlH_4$ system. This stabilization could be related to the conformational changes induced in the RS and TS by the solvent. The RS structures for both complexes have similar conformations to the TS structures in THF, while the PS structures are significantly different from the TS due to structural relaxation, as was also observed under vacuum.

From the above, we confirmed that the calculated energies and geometries of the RS, TS and PS were consistent with those determined in previous studies. We next

investigated changes in the structure and energy during the hydride transfer process in detail, using the rearrangement parameter; α, and the relative energies of the RS along the IRC. From this, the H atom transfer mechanism during the hydride transfer process was elucidated. Herein, the transferred H atom is denoted by ‘H’, which is not distinguished from the hydride ion (H^-), hydrogen atom (H) and proton (H^+). Figures 6.5 and 6.6 summarize the values of α and the relative energies of the RS along the IRC for $LiAlH_4$ and $LiBH_4$-formaldehyde complexes under vacuum and in THF. From these figures it is evident that α is not varied by the presence or absence of THF for the LiAlH4 system, and remains at 0 up to the point at which the TS appears. These data indicate that the TS exists as a reactant-like structure in this chemical reaction. Once the ‘H’ has completely transferred to the carbonyl carbon, the energy decreases drastically and the structure changes to the PS due to structural relaxation, moving from IRC = 7 to 15.

Conversely, in the case of the $LiBH_4$ system, different values of α were found depending on the presence of the solvent. With THF, the α value at the RS has already exceeded 0.5, signifying that the ‘H’ transfer is more than halfway complete. The change in α at the RS can be explained by the conformational changes resulting from charge responses to the solvent effect. Thus, the carbonyl carbon more closely approaches the boron in the RS in THF because a Li-O-C bond is generated by the

solvent effect. In the case of both vacuum and THF conditions, the ‘H’ transfer to the carbonyl carbon initiates prior to passing the TS, such that the transfer is complete just before formation of the TS (IRC = 0), corresponding to a product-like structure. When using $LiBH_4$, once the ‘H’ has completely transferred to the carbonyl carbon, as is also the case with $LiAlH_4$, the energy has decreased and the structure changes to the PS due to structural relaxation.

Comparing the mechanisms of both complexes moving from the RS to TS, we determined that the ‘H’ transfer in the case of $LiAlH_4$ begins in the vicinity of the TS, and thus can be considered an early barrier reaction, while the ‘H’ transfer with $LiBH_4$ had finished in the vicinity of the TS, indicating a late barrier reaction. These results are consistent with the Hammond postulate [145] based on the fact that a TS structure having a low activation energy is reactant-like, while a structure with a high activation energy is product-like. The data indicate that the rate determine step in the hydride transfer is different when using $LiAlH_4$ compared to the use of $LiBH_4$.

Finally, to clarify the charge transfer dynamics, we calculated the changes in charge density during the hydride transfer process along the IRC. Charge densities were obtained by considering four fragments: CH_2O, AlH_3 or BH_3, ‘H’ and Li^+. Figures 6.7 and 6.8 show the charge density results obtained for the $LiAlH_4$ and $LiBH_4$-formaldehyde complexes under vacuum and in THF, respectively. The charge density for Li^+ was

not plotted in these figures because, for both $LiAlH_4$ and $LiBH_4$, the Li^+ charge was invariant over the course of the reaction. In either system, the negative charge of the CH_2O fragment is seen to increase, while that of the AlH_3 or BH_3 decreases during ‘H’ transfer. These results indicate electron transfer from the AlH_3 or BH_3 fragment to CH_2O during the ‘H’ transfer.

We subsequently focused on the charge density of the $LiAlH_4$ system under vacuum, because the solvent effect was not observed in the case of the charge density for this system. The charge transfer parameter for the CH_2O fragment was estimated so as to clearly understand the relationship between the ‘H’ and electron transfers. This parameter was calculated by setting the charges at the RS and PS to 0 and 1, respectively. Figure 6.9 summarizes the variations in the rearrangement and charge transfer parameter with IRC. From Fig. 6.9(a), it can be seen that the charge transfer parameter increases prior to the ‘H’ transfer, suggesting that a one electron transfer occurs before the ‘H’ transfer. Figure 6.7(a) shows that the negative charge of the CH_2O fragment increases during the ‘H’ transfer, while the negative charge of the transferring ‘H’ gradually decreases. Therefore, the ‘H’ transfers to the carbonyl carbon along with the electron transfer. We also calculated the bond order of the Al-H and C-H bonds to investigate the behavior of the chemical bond during hydride transfer. The calculated bond orders for Al-H and C-H were 0.73 and 0.00 at the RS, but 0.57

and 0.28 at the TS, respectively. These results indicate that an Al-H-C bond is formed as the one electron transfer takes place prior to the 'H' transfer. In summary, hydride transfer using $LiAlH_4$ proceeds as follows: (1) a one electron transfer to the carbonyl carbon occurs, (2) a bridge bond (the Al-H-C bond) forms, (3) the 'H' transfer begins, with electron transfer as the driving force, and finally (4) a single electron subsequently moves gradually toward the carbonyl carbon through the Al-H-C bond while the 'H' transfers.

In the case of $LiBH_4$, a solvent effect on the charge density was observed. The changes in charge could be explained by conformational changes of the RS and TS structures by solvent effects. We estimated the charge transfer parameter in the same manner as for the $LiAlH_4$ system. Figure 6.9(b) shows that the negative charge of the CH_2O fragment increases before the 'H' transfer, which is the same result as obtained with $LiAlH_4$. The bond order calculated for B-H and C-H were 0.78 and 0.00 at the RS, and 0.71 and 0.26 at IRC = 5, respectively. From these results, we found that a B-H-C bond was formed via one electron transfer in advance of the 'H' transfer, just as with $LiAlH_4$. In summary, we found that the essential mechanism of the hydride transfer using $LiBH_4$ was the same as that when using $LiAlH_4$.

From these charge density analyses, we ascertained that the relationship between charge transfer and hydride transfer is the same when employing either $LiAlH_4$ or

$LiBH_4$. However, the TS structures in both systems are different, representing reactant-like and product-like structures, respectively. By comparing the TS structures of both systems, we also found that the rate-determining steps in the hydride transfer are one electron transfer to the carbonyl carbon for the $LiAlH_4$ system, and B-H bond dissociation for the $LiBH_4$ system. The presence of THF affects the structure and energy values throughout the reaction by influencing charge separation, although the hydride transfer and the charge are not affected by the solvent.

6.4 Conclusion

We studied the differences in the geometry of the RS, TS and PS under vacuum and in THF as well as the dynamic changes associated with the transfer of the H atom and the charge density along the reaction coordinate for the reduction of formaldehyde by $LiAlH_4$ or $LiBH_4$, using DFT calculations. We obtained information about the hydride transfer mechanism that allowed us to investigate the behavior of the hydride and the charge density along the IRC. The resulting data indicated that Li^+ contributes to the stabilization of the TS, and this effect is more pronounced in the presence of a solvent. The TS structure associated with the $LiAlH_4$-fomaldehyde complex is reactant-like, while the $LiBH_4$ structure is product-like. These results are consistent with the

Hammond postulate, because the activation energy for the $LiAlH_4$ system is lower than that for $LiBH_4$. Although these results are also in agreement with various previous reports, the work presented herein goes further so as to allow a detailed understanding of the hydride transfer mechanism based on our computational results for the geometries, energies and charge densities and comparison of both systems.

The essential mechanism of the hydride transfer is the same for both reducing agents, and may be summarized as follows: (1) one electron transfer to the carbonyl carbon, (2) formation of a bridge bond (X-H-C bond; X = Al or B), (3) initiation of ' H ' transfer driven by electron transfer and (4) one electron flow through the X-H-C bond in conjunction with transfer of the ' H ', during which the hydrogen atom or proton-coupled electron transfer occurs. The presence of a solvent affects the structure and energy values through charge separation, but has no effect on the hydride transfer and charge. Finally, this study suggests that the rate-determining steps in the hydride transfer when employing $LiAlH_4$ and $LiBH_4$ are one electron transfer to the carbonyl carbon and B-H bond dissociation, respectively.

Table 6.1: Activation energy (ΔE_a) and energy difference (ΔE) between reactant and product states for hydride transfer in the vacuum state.

Hydride reagent	ΔE_a (kJ/mol)	ΔE (kJ/mol)
AlH_4^-	49.9	-189
LiAlH4	10.1	-196
BH_4^-	144.9	-121
$LiBH_4$	80.8	-117

Table 6.2: Calculated Bond lengths (Å), Angles (deg), Dihedral angles (deg) with hydride transfer of TS, and activation energy ΔE_a, and energy difference ΔE in Explicit model and PCM for $LiAlH_4$ system.

		Explicit model	PCM
Length (Å)	Al-H	1.67	1.66
	C-H	1.82	1.79
Angle (deg)	Al-H-C	118	133
Dihedral angle (deg)	Al-H-C-O	25	4
ΔE_a (kJ/mol)		6.51	2.37
ΔE (kJ/mol)		-199	-224

Table 6.3: Total energies of the RS, TS and PS and activation energy (ΔE_a) and energy difference (ΔE) between the RS and PS for hydride transfer.

Hydride reagent	Solvent	E (a.u.)			*ΔEa* (kJ/mol)	*ΔE* (kJ/mol)
		RS	TS	PS		
$LiAlH_4$						
	Vacuum	-366.88584	-366.88201	-366.96052	10.1	-196
	THF (ε^b=7.58)	-366.91245	-366.91155	-366.99774	2.37	-224
$LiBH_4$						
	Vacuum	-149.29184	-149.26107	-149.33650	80.8	-117
	THF (ε=7.58)	-149.30878	-149.29741	-149.37483	30.0	-173

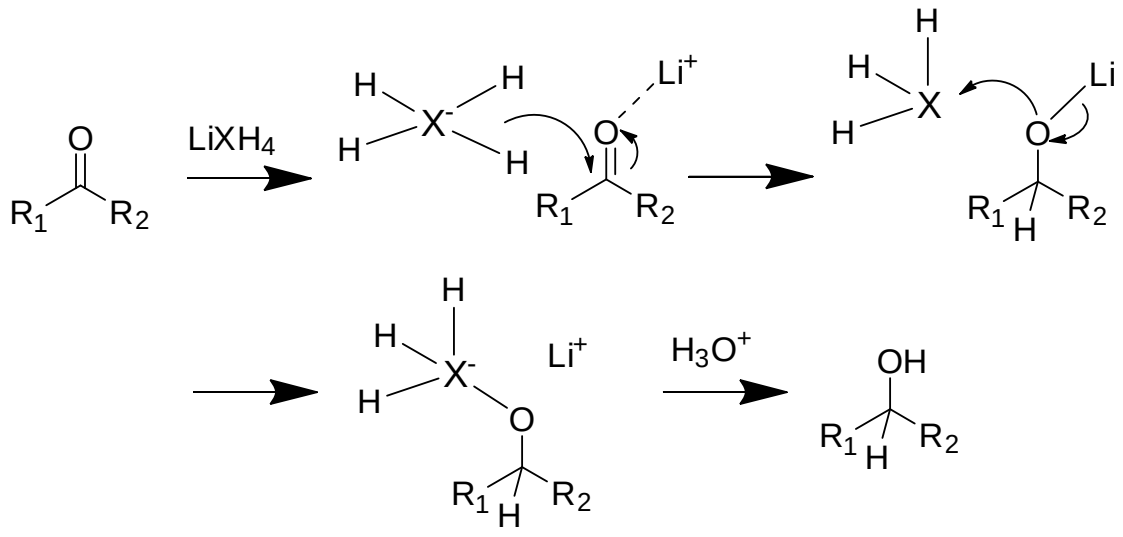

Figure 6.1: The generally supported hydride reduction mechanism.

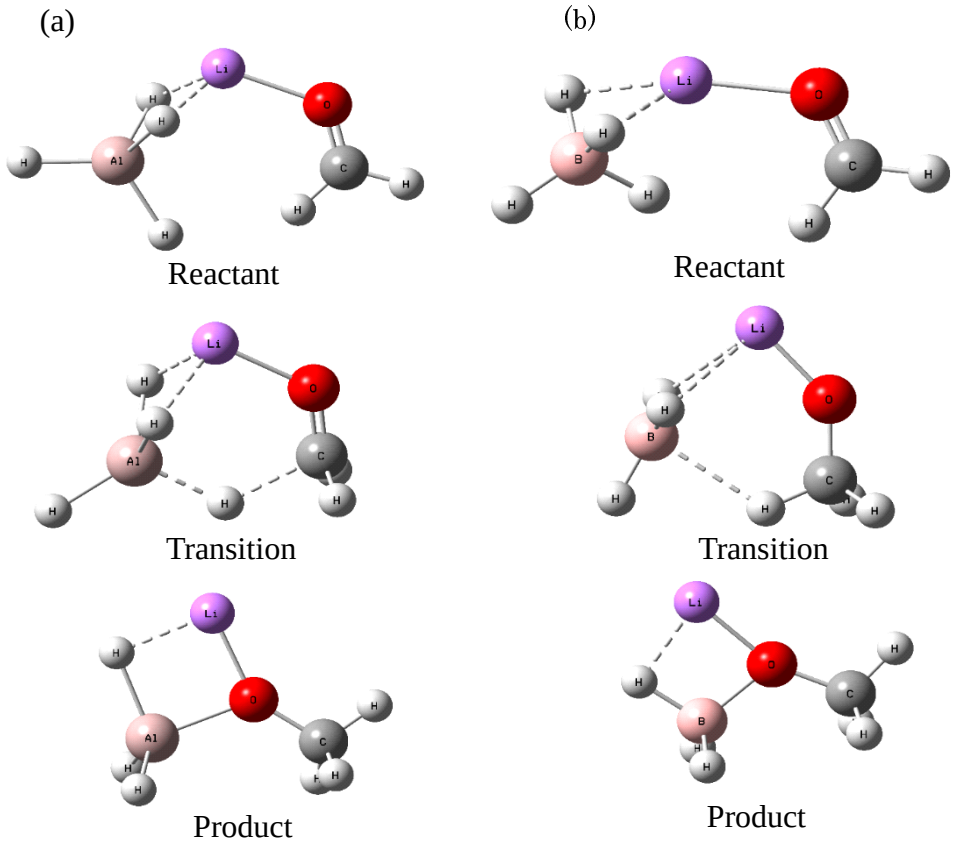

Figure 6.2: Reactant, transition and product state structures for hydride transfer of (a) $LiAlH_4$- and (b) $LiBH_4$-formaldehyde complexes in the vacuum state.

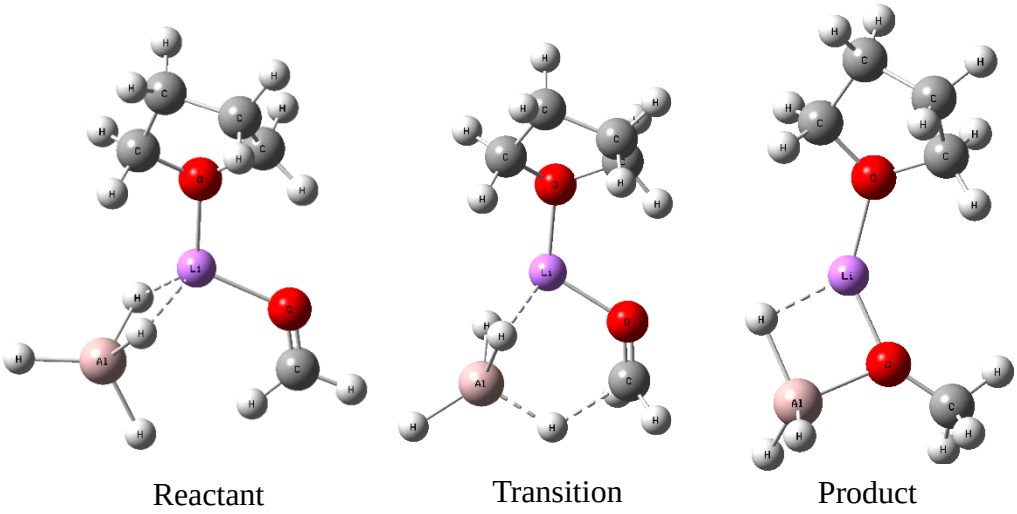

Figure 6.3: Reactant, transition and product state structures for hydride transfer of $LiAlH_4$-formaldehyde complexes including one explicit THF molecule. (This calculation is carried out using Aug-cc-pVDZ basis set.)

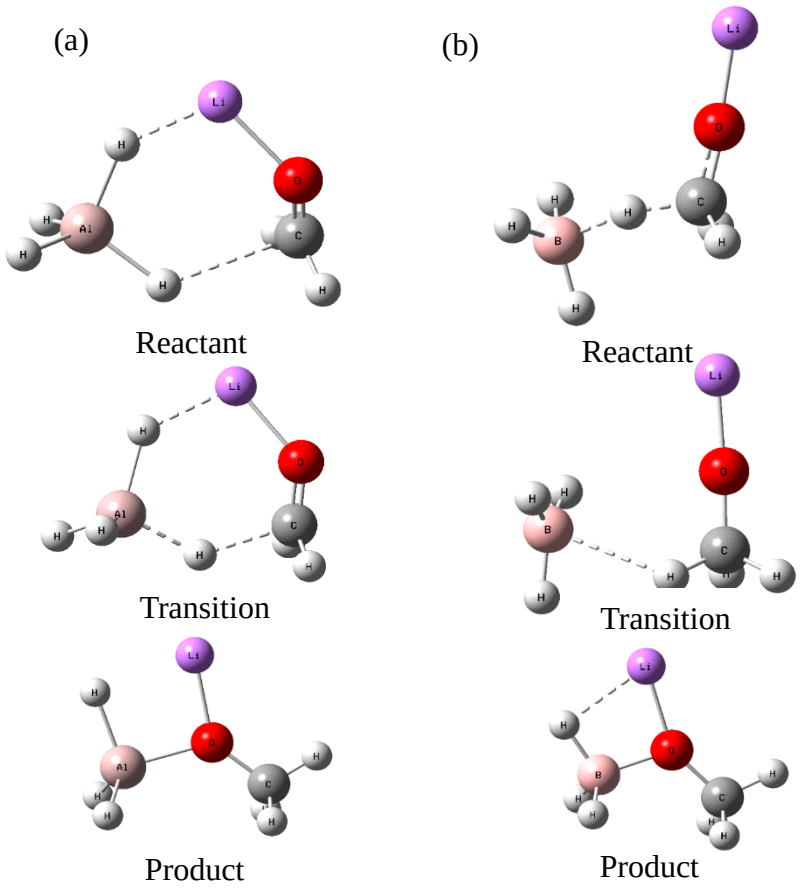

Figure 6.4: Reactant, transition and product state structures for hydride transfer of (a) $LiAlH_4$- and (b) $LiBH_4$-formaldehyde complexes in THF.

(a) $LiAlH_4$

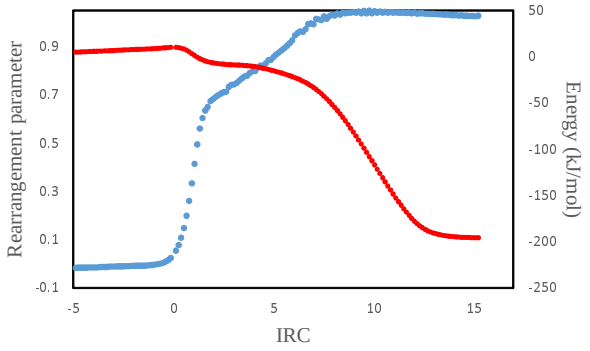

(b) $LiBH_4$

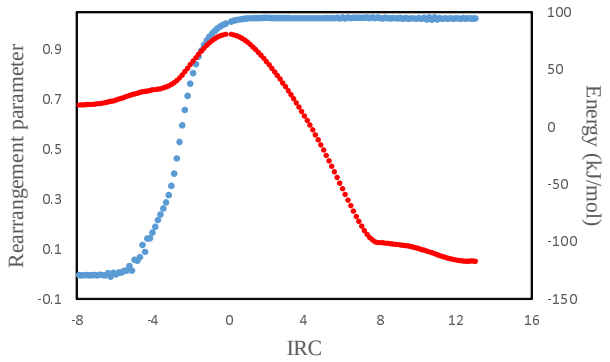

Figure 6.5: Rearrangement parameter values (blue) and relative energies (red) for the RS along the IRC for the (a) $LiAlH_4$- and (b) $LiBH_4$-formaldehyde complexes in the vacuum state.

(a) $LiAlH_4$

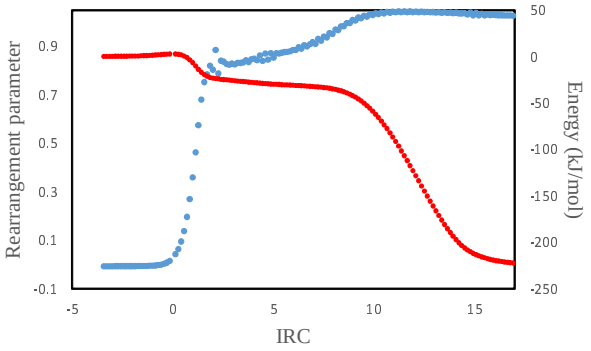

(b) $LiBH_4$

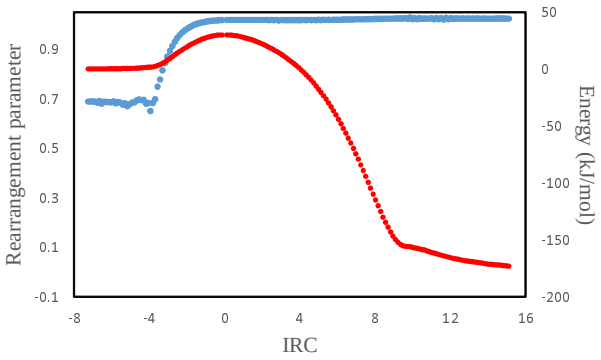

Figure 6.6: Rearrangement parameter values (blue) and relative energies (red) for the RS along the IRC for the (a) $LiAlH_4$- and (b) $LiBH_4$-formaldehyde complexes in THF.

(a) $LiAlH_4$

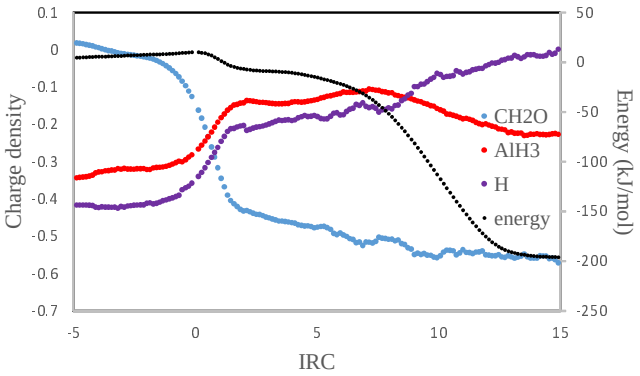

(b) $LiBH_4$

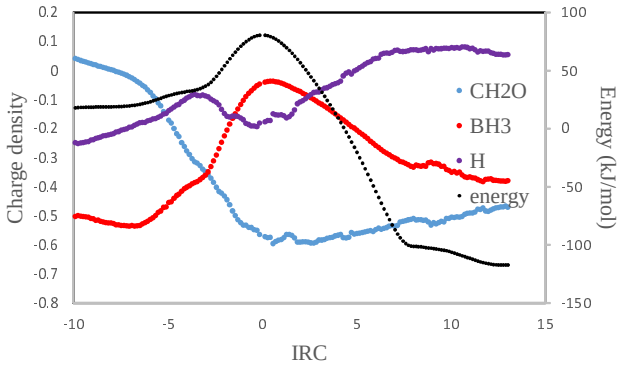

Figure 6.7: Charge densities of CH_2O (blue), AlH_3 (red) and H (purple) and energy values (black) along the IRC for the (a) $LiAlH_4$- and (b) $LiBH_4$-formaldehyde complexes under vacuum.

(a) $LiAlH_4$

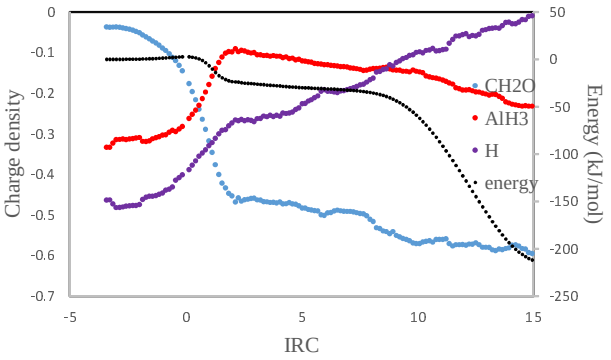

(b) $LiBH_4$

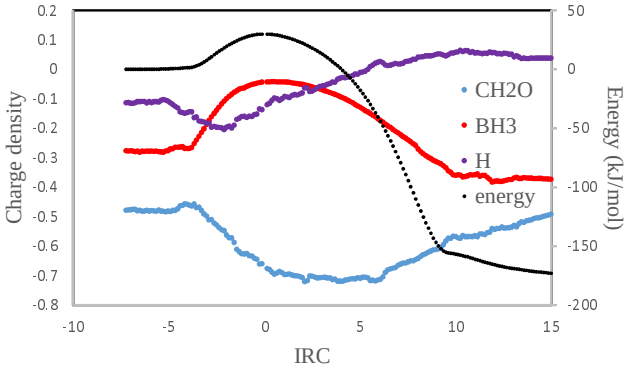

Figure 6.8: Charge densities of CH_2O (blue), BH_3 (red) and H (purple) and energy values (black) along the IRC for the (a) $LiAlH_4$- and (b) $LiBH_4$-formaldehyde complexes in THF.

(a) $LiAlH_4$

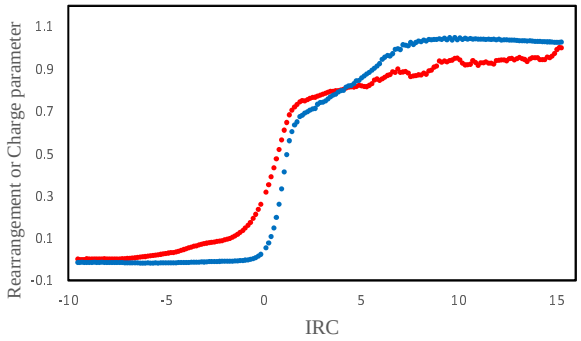

(b) $LiBH_4$

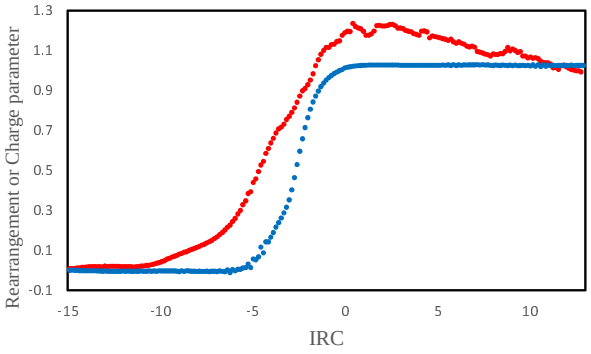

Figure 6.9: Rearrangement (blue) and charge transfer parameters (red) for (a) $LiAlH_4$ and (b) $LiBH_4$ under vacuum.

Chapter 7

Conclusion

Potential energy surface (PES) is an important theoretical approach for understanding chemical reactions. Once the PES is obtained, the analysis of the reactions such as determination of rate constants and reaction path can be performed using the PES. In addition, the quantum effect of nucleus in the reaction, which is important for proton transfer, can be treated using quantum dynamics simulation on the PES. Therefore, to investigate the chemical reaction mechanism, it is important work to construct the PES and perform the quantum dynamics simulation on the PES, which possesses a number of attractive features for various molecular systems.

In this dissertation, a simple construction method of global PES and analytical method using the PES for intermolecular proton transfer were discussed. Chapter 3 was found that PES for intermolecular proton transfer could be constructed by using Morse potential as the diagonal matrix elements and Gaussian function as the non-diagonal

matrix element in the diabatic picture. In addition, a simple method to uniquely construct the diabatic potentials was proposed using these analytical functions. In chapter 4, a simple thermal rate constant estimation method for using a quantum dynamics simulation on the diabatic potentials were proposed. The proton transfer rate constants determined by this approach were in good agreement with the reference values. Furthermore, since this approach can be performed easily for homo- and hetero-molecular pairs, it can be applied to intermolecular proton transfer estimations for various large molecular systems. Therefore this approach was applied to the proton transfer in proton conductive material in chapter 5. The results showed that the proton diffusion path in this material in terms of local proton transfer. Finally a detailed analysis of hydride transfer using adiabatic potential was discussed in chapter 6. The analysis using IRC was found that the change in geometries, solvent effect, and charge transfer process in detail during the hydride transfer process.

From the above, it was concluded that an analytical approach to various proton transfer systems using PES, especially diabatic picture, was developed.

Acknowledgements

I would like to express my special appreciation and thanks to my dissertation advisor Associate Professor Tomonori Ida. I would like to thank you for encouraging my research and for allowing me to grow as a research scientist. His advice on both research as well as on my career have been priceless.

I would also like to express my very sincere gratitude to Professor Professor Motohiro Mizuno for collaboration and fruitful discussion throughout my study and the support to make this dissertation possible.

I am thankful to Assistant Professor Ryutaro Ohashi for the support and encouragement whenever I was in need.

I am thankful to all the members of the theoretical chemistry laboratory, Kanazawa University, for the friendship and spiritual support.

I would also like to thank all of my friends who supported me in writing, and incented me to strive towards my goal.

Last but not the least, I would like to thank my parents for giving birth to me and supporting me spiritually throughout my life. I would also like to thank my sister for support and encouragement throughout my life.

References

[1] D. G. Truhlar, R. Steckler, M. S. Gordon, *Chem. Rev.,* **87**, 217, (1987).

[2] G. C. Schatz, *Rev. Mod. Phys.,* **61**, 669, (1989).

[3] R. D. Levine, *Molecular Reaction Dynamics,* Cambridge University Press. (2009).

[4] T. V. Voorhis, T. Kowalczyk, B. Kaduk, L.-P. Wang, C.-L. Cheng, Q. Wu, *Annu. Rev. Phys. Chem.,* **61**, 149, (2010).

[5] J. Åqvist, A. Warshel, *Chem. Rev.,* **93**, 2523, (1993).

[6] Y. Mo, J. Gao, *J. Phys. Chem. A,* **104**, 3012, (2000).

[7] D. G. Truhlar, *J. Comp. Chem.,* **28**, 73, (2007).

[8] L. Song, J. Gao, *J. Phys. Chem. A,* **112**, 12925, (2008).

[9] A. Warshel, R. M. Weiss, *J. Am. Chem. Soc.,* **102**, 6218, (1980).

[10] J. Lobaugh, G. A. Voth, *J. Chem. Phys.,* **104**, 2056, (1996).

[11] A. Warshel, R. M. Weiss, *J. Am. Chem. Soc.,* **102**, 6218, (1980).

[12] Y.-T. Chang, W. H. Miller, *J. Phys. Chem.,* **94**, 5884, (1990).

[13] K. Hinsen, B. Roux, *J. Comp. Chem.,* **18**, 368, (1997).

[14] C. Minichino, G. A. Voth, *J. Phys. Chem. B,* **101**, 4544, (1997).

[15] D. E. Sagnella, M. E. Tuckerman, *J. Chem. Phys.,* **108**, 2073, (1998).

[16] R. Vuilleumier, D. Borgis, *Chem. Phys. Lett.,* **284**, 71, (1998).

[17] Y. Wang, J. R. Gunn, *Int. J. Quant. Chem.,* **73**, 357, (1999).

[18] U. W. Schmitt, G. A. Voth, *J. Chem. Phys.,* **111**, 9361, (1999).

[19] M. Čuma, U. W. Schmitt, G. A. Voth, *Chem. Phys.,* **258**, 187, (2000).

[20] M. Čuma, U. W. Schmitt, G. A. Voth, *J. Phys. Chem. A,* **105**, 2814, (2001).

[21] G. Brancato, M. E. Tuckerman, *J. Chem. Phys.,* **122**, 224507, (2005).

[22] G. Hong, E. Rosta, A. Warshel, *J. Phys. Chem. B,* **110**, 19570, (2006).

[23] S. Lammers, S. Lutz, M. Meuwly, *J. Comp. Chem.,* **29**, 1048, (2008).

[24] H. Chen, T. Yan, G. A. Voth, *J. Phys. Chem. A,* **113**, 4507, (2009).

[25] S. Feng, G. A. Voth, *J. Phys. Chem. B,* **115**, 5903, (2011).

[26] S. C. L. Kamerlin, A. Warshel, *IREs. Comput. Mol. Sci.,* **1**, 30, (2011).

[27] A. Li, Z. Cao, Y. Li, T. Yan, P. Shen, *J. Phys. Chem. B,* **116**, 12793, (2012).

[28] T. Seideman, W. H. Miller, *J. Chem. Phys.,* **96**, 4412, (1992).

[29] T. Seideman, W. H. Miller, *J. Chem. Phys.,* **97**, 2499, (1992).

[30] W. H. Miller, *Acc. Chem. Res.,* **26**, 174, (1993).

[31] C. J. Cramer, *Essentials of Computational Chemistry, Theories and Models, Second Edition,* (Wiley, England, 2004).

[32] F. Jensen, *Introduction to Computational Chemistry,* (Wiley, England, 1999).

[33] I. N. Levine, *QUANTUM CHEMISTRY,* Sixth Edition, (Pearson Education, 2008).

[34] A. D. Becke, *J. Chem. Phys.,* **140**, 18A301, (2014).

[35] P. Hohenberg, W. Kohn, *Phys. Rev.,* **136**, B864, (1964).

[36] W. Kohn, L. J. Sham, *Phys. Rev. B.,* **140**, 1133, (1965).

[37] P. A. M. Dirac, *Proc. Cambridge Phil. Soc.,* **26**, 376, (1930).

[38] A. D. Becke *Phys. Rev. B,* **38**, 3098, (1988).

[39] C. Lee, W. Yang, R. G. Parr, *Phys. Rev. B,* **37**, 785, (1988).

[40] P. J. Stephens, F. J. Devlin, C. F. Chabalowski, and M. J. Frisch, *J. Chem. Phys.,* **98**, 11623, (1994).

[41] T. Yanai, D. Tew, and N. Handy, *Chem. Phys. Lett.,* **393**, 51, (2004).

[42] W. D. Arnold, L. K. Sanders, M. T. Mcmahon, A. V. Volkov, G. Wu, P. Coppens, S. R. Wilson, N. Godbout, E. Oldfield, *J. Am. Chem. Soc.,* **122**, 4708, (2000).

[43] Y. Wang, X. Cheng, X. Yang, X. Yang, *J. Sol. Chem.,* **35**, 869, (2006).

[44] R. Kobayashi, R. D. Amos, *Chem. Phys. Lett.,* **420**, 106, (2006).

[45] P. A. Limacher, K. V. Mikkelsen, H. P. Lüthi, *J. Chem. Phys.,* **130**, 194114, (2009).

[46] S. Zhang, Z. Qu, P. Tao, B. Brooks, Y. Shao, X. Chen, C. Liu, *J. Phys. Chem. C,* **116**, 12434, (2012).

[47] H. Eyring, *J. Chem. Phys.,* **3**, 107, (1935).

[48] M. G. Evans, M. Polanyi, *Trans. Faraday. Soc.,* **31**, 875, (1935).

[49] J. Z. H. Zhang, *Theory and Application of Quantum Molecular Dynamics.* (World Scientific: Singapore, 1999).

[50] G. Nyman, H.-G. Yu, *Int. Rev. Phys. Chem.,* **32**, 39, (2013).

[51] D. J. Tannor, *Introduction to Quantum Mechanics: A Time-Dependent Perspective.* (Univ Science Books, 2006).

[52] L. Jaroszewski, B. Lesyng, J. J. Tanner, J. A. McCammon, *Chem. Phys. Lett.,* **175**, 282, (1990).

[53] L. Jaroszewski, B. Lesynga, J. A. McCammon, *J. Mol. Struct. (THEOCHEM),* **283**, 57, (1993).

[54] W. Tatara, M. J. Wójcik, J. Lindgren, M. Probstet, *J. Phys. Chem. A,* **107**, 7827, (2003).

[55] G. F. Mangiatordi, J. Hermet, C. Adamoet, *J. Phys. Chem. A,* **115**, 2627, (2011).

[56] Gaussian 09, Revision D.01, M. J. Frisch, G. W. Trucks, H. B. Schlegel, G. E. Scuseria, M. A. Robb, J. R. Cheeseman, G. Scalmani, V. Barone, B. Mennucci, G. A. Petersson, H. Nakatsuji, M. Caricato, X. Li, H. P. Hratchian, A. F. Izmaylov, J. Bloino, G. Zheng, J. L. Sonnenberg, M. Hada, M. Ehara, K. Toyota, R. Fukuda, J. Hasegawa, M. Ishida, T. Nakajima, Y. Honda, O. Kitao, H. Nakai, T. Vreven, J. A. Montgomery, Jr., J. E. Peralta, F. Ogliaro, M. Bearpark, J. J. Heyd, E. Brothers, K. N. Kudin, V. N. Staroverov, R. Kobayashi, J. Normand,

K. Raghavachari, A. Rendell, J. C. Burant, S. S. Iyengar, J. Tomasi, M. Cossi, N. Rega, J. M. Millam, M. Klene, J. E. Knox, J. B. Cross, V. Bakken, C. Adamo, J. Jaramillo, R. Gomperts, R. E. Stratmann, O. Yazyev, A. J. Austin, R. Cammi, C. Pomelli, J. W. Ochterski, R. L. Martin, K. Morokuma, V. G. Zakrzewski, G. A. Voth, P. Salvador, J. J. Dannenberg, S. Dapprich, A. D. Daniels, Ö. Farkas, J. B. Foresman, J. V. Ortiz, J. Cioslowski, D. J. Fox, Gaussian, Inc., Wallingford CT, (2009).

[57] W. H. Miller, B. M. D. D. op de Haar, *J. Phys. Chem.,* **86**, 6213, (1987).

[58] J. Z. H. Zhang, S.-I. Chu, W. H. Miller, *J. Chem. Phys.,* **88**, 6233, (1988).

[59] J. Z. H. Zhang, D. J. Kouri, K. Haug, D. W. Schwenke, Y. Shima, D. G. Truhlar, *J. Chem. Phys.,* **88**, 2492, (1988).

[60] F. Webster, J. C. Light, *J. Chem. Phys.,* **90**, 265, (1989).

[61] S. Shin, J. C. Light, *J. Chem. Phys.,* **101**, 2836, (1994).

[62] L. Wang, *Chem. Phys.,* **237**, 305, (1998).

[63] C. Shin, S. Shin, *J. Chem. Phys.,* **113**, 6528, 2000.

[64] T.-S. Chu, K.-L. Han, M. Hankel, G. G. Balint-Kurti, A. Kuppermann, R. Abrol, *J. Chem. Phys.,* **130**, 1, (2009).

[65] T.-S. Chu, Y. Zhang, K.-L. Han, *Int. Rev. Phys. Chem.,* **25**, 201, (2006).

[66] T.-S. Chu, K.-L. Han, *Phys. Chem. Chem. Phys.,* **10**, 2431, (2008).

[67] D. J. Tannor, D. E. Weeks, *J. Chem. Phys.,* **98**, 3884, (1993).

[68] D. E. Weeks, D. J. Tannor, *Chem. Phys. Lett.,* **207**, 301, (1993).

[69] S. Garashchuk, D. Tannor, *Chem. Phys. Lett.,* **262**, 477, (1996).

[70] S. Garashchuk, D. J. Tannor, *J. Chem. Phys.,* **109**, 3028, (1998).

[71] S. Garashchuk, D. J. Tannor, *J. Chem. Phys.,* **110**, 2761, (1999).

[72] F. Grossmann, E. J. Heller, *Chem. Phys. Lett.,* **241**, 45, (1995).

[73] D. H. Zhang, J. C. Light, *J. Chem. Phys.,* **104**, 6184, (1996).

[74] Y. Yoon, C. Shin, S. Shin, *Chem. Phys.,* **326**, 425, (2006).

[75] H. Park, C. Shin, S. Shin, *Bull. Korean Chem. Soc.,* **35**, 1061, (2014).

[76] G.-J. Zhao, K.-L. Han, *Acc. Chem. Res.,* **45**, 404, (2012).

[77] K. Pogorzelec-Glaser, J. Garbarczyk, C. Pawlaczyk, E. Markiewicz, *Mater. Sci.-Poland,* **24**, 245, (2006).

[78] K. Pogorzelec-Glaser, C. Pawlaczyk, A. Pietraszko, E. Markiewicz, *J. Power Sources,* **173**, 800, (2007).

[79] R. Vuilleumier, D. Borgis, *J. Mol. Struct.,* **552**, 117, (2000).

[80] H.-P. Cheng, *J. Chem. Phys.,* **105**, 6844, (1996).

[81] W. Münch, K. D. Kreuer, W. Silvestri, J. Maier, G. Seifert, *Solid State Ionics,* **145**, 437, (2001).

[82] T. Umiyama, R. Ohashi, T. Ida, M. Mizuno, *Chem. Lett.,* **42**, 1323, (2013).

[83] M. Kumar, A. Venkatnathan, *J. Phys. Chem. B,* **119**, 3213, (2015).

[84] K. D. Kreuer, A. Fuchs, M. Ise, M. Spaeth, J. Maier, *Electrochim. Acta,* **43**, 1281, (1998).

[85] A. Bozkurt, W. H. Meyer, *Solid State Ionics,* **138**, 259, (2001).

[86] F. Sevil, A. Bozkurt, *J. Phys. Chem. Solids,* **65**, 1659, (2004).

[87] M. Yamada, I. Honma, *Polymer,* **45**, 8349, (2004).

[88] M. Yamada, I. Honma, *Polymer,* **46**, 2986, (2005).

[89] Z. Zhou, S. Li, Y. Zhang, M. Liu, W. Li, *J. Am. Chem. Soc.,* **127**, 10824, (2005).

[90] S. Li, Z. Zhou, Y. Zhang, M. Liu, *Chem. Mater.,* **17**, 5884, (2005).

[91] M. Kufacı, A. Bozkurt, M. Tülü, *Solid State Ionics,* **177**, 1003, (2006).

[92] H. Pu, D. Wang, *Electrochim. Acta,* **51**, 5612, (2006).

[93] S. R. Narayanan, S. P. Yen, L. Liu, S. G. Greenbaum, *J. Phys. Chem. B,* **110**, 3942, (2006).

[94] S. Bureekaew, S. Horike, M. Higuchi, M. Mizuno, T. Kawamura, D. Tanaka, N. Yanai, S. Kitagawa, *Nat. Mater.,* **8**, 831, (2009).

[95] S. Ü. Çelik, A. Bozkurt, S. S. Hosseini, *Prog. Polym. Sci.,* **37**, 1265, (2012).

[96] A. Kawada, A. R. McGhie, M. M. Labes, *J. Chem. Phys.,* **52**, 3121, (1970).

[97] B. S. Hickman, M. Mascal, J. J. Titman, I. G. Wood, *J. Am. Chem. Soc.,* **121**, 11486, (1999).

[98] I. Fischbach, H. W. Spiess, K. Saalwa, G. R. Goward, *J. Chem. Phys. B,* **108**, 18500, (2004).

[99] M. Iannuzzi, M. Parrinello, *Phys. Rev. Lett.,* **93**, 1, (2004).

[100] M. Iannuzzi, *J. Chem. Phys.,* **124**, 204710, (2006).

[101] N. C. Deno, H. J. Peterson, G. S. Saines, *Chem. Rev.,* **60**, 7, (1960).

[102] C. Ian, F. Watt, *Adv. Phys. Org. Chem.,* **24**, 57, (1988).

[103] J. Clayden, N. Greeves, S. Warren, P. Wothers, *Organic Chemistry,* Oxford University Press, 2001.

[104] Y. Murakami, J.-I. Kikuchi, Y. Hisaeda, O. Hayashida, *Chem. Rev.,* **96**, 721, (1996).

[105] P. F. Fitzpatrick, *Acc. Chem. Res.,* **34**, 299, (2001).

[106] B. Y. Hong, M. Haddad, F. Maley, J. H. Jensen, A. Kohen, *J. Am. Chem. Soc.,* **128**, 5636, (2006).

[107] P. Neta, *Chem. Rev.,* **72**, 533, (1972).

[108] J.-S. Song, D. J. Szalda, R. M. Bullock, *Organometallics,* **20**, 3337, (2001).

[109] P. L. Gaus, S. C. Kao, K. Youngdahl, M. Y. Darensbourg, *J. Am. Chem. Soc.,* **107**, 2428, (1985).

[110] R. M. Bullock, J.-S. Song, *J. Am. Chem. Soc.,* **116**, 8602, (1994).

[111] S. C. Kao, C. T. Spillett, C. Ash, R. Lusk, Y. K. Park, M. Y. Darensbourg, *Organometallics,* **4**, 83, (1985).

[112] M. P. Magee, J. R. Norton, *J. Am. Chem. Soc.,* **123**, 1778, (2001).

[113] O. Tapia, J. Andres, J. M. Aullo, C.-I. Bränden, *J. Chem. Phys.,* **83**, 4673, (1985).

[114] O. Tapia, J. Andres, J. M. Aullo, R. Cardenas, *J. Mol. Struct., Theochem,* **167**, 395, (1988).

[115] J. Mestres, A. Lledo's, M. Duran, J. Bertra'n, *J. Mol. Struct., Theochem,* **260**, 259, (1992).

[116] J. Mestres, M. Duran, J. Bertra'n, *Theor. Chim. Acta,* **88**, 325, (1994).

[117] J. Mestres, M. Duran, J. Bertra'n, *Bioorganic Chemistry,* **80**, 69, (1996).

[118] X. Fradera, M. Duran, J. Mestres, *Can. J. Chem.,* **78**, 328, (2000).

[119] X. Q. Zhu, Y. Liu, B. J. Zhao, J. P. Cheng, *J. Org. Chem.,* **66**, 370, (2001).

[120] J. Gębicki, A. Marcinek, J. Zielonka, *Acc. Chem. Res.,* **37**, 379, (2004).

[121] A. N. Pankratov, B. I. Drevko, *J. Serb. Chem. Soc.,* **69**, 431, (2004).

[122] H. Buck, *Int. J. Quant. Chem.,* **101**, 389, (2005).

[123] A. N. Pankratov, B. I. Drevko, *Chemistry of Heterocyclic Compounds,* **41**, 1105, (2005).

[124] S. Khanna, D. Kaur, R. Kaur, *J. Phys. Org. Chem.,* **27**, 747, (2014).

[125] M. F. Powell, J. C. Wu, T. C. Bruice, *J. Am. Chem. Soc.,* **106**, 3850, (1984).

[126] L. L. Miller, J. R. Valentine, *J. Am. Chem. Soc.,* **110**, 3982, (1988).

[127] M. F. Powell, T. C. Bruice, *J. Am. Chem. Soc.,* **105**, 1014, (1983).

[128] J.-P. Cheng, Y. Lu, X. Zhu, L. Mu, *J. Org. Chem.,* **63**, 6108, (1998).

[129] X. Q. Zhu, Y. C. Liu, J. P. Cheng, *J. Org. Chem.,* **64**, 8980, (1999).

[130] E. C. Ashby, F. R. Dobbs, H. P. Hopkins, *J. Am. Chem. Soc.,* **97**, 3158, (1975).

[131] E. C. Ashby, J. R. Boone, *J. Am. Chem. Soc.,* **98**, 5524, (1976).

[132] R. T. Luibrand, I. R. Taigounov, A. A. Taigounov, *J. Org. Chem.,* **66**, 7254, (2001).

[133] D. E. Bikiel, F. D. Salvo, M. C. G. Lebrero, F. Doctorovich, D. A. Estrin, *Inorg. Chem.,* **44**, 5286, (2005).

[134] D. C. Wigfield, *Tetradedron,* **35**, 449, (1979).

[135] R. Bonaccorsi, P. Palla, J. Tomasi, *J. Mol. Struct., Theochem,* **87**, 181, (1982).

[136] R. Bonaccorsi, R. Clmiraglia, J. Tomasi, S. Miertuš, *J. Mol. Struct., Theochem,* **94**, 11, (1983).

[137] M. J. S. Dewar, M. L. McKee, *J. Am. Chem. Soc.,* **100**, 7499, (1978).

[138] Y. Suzuki, D. Kaneno, S. Tomoda, *J. Phys. Chem. A,* **113**, 2578, (2009).

[139] H. Yamataka, T. Hanafusa, *J. Am. Chem. Soc.,* **108**, 6643, (1986).

[140] M. Najafi, M. Zahedi, E. Klein, *Comp. Theor. Chem.* **978**, 16, (2011).

[141] E. Sigfridsson, U. Ryde, *J. Comp. Chem.,* **19**, 377, (1998).

[142] G. S. Maciel, E. Garcia, *Chem. Phys. Lett.,* **409**, 29, (2005).

[143] F. Martin, H. Zipse, *J. Comp. Chem.,* **26**, 97, (2005).

[144] K. Hu, L. Wang, X. Liu, Q. Zhuang, Z. Xue, Z. Han, *Comp. Theor. Chem.,* **1042,** 1, (2014).

[145] G. S. Hammond, *J. Am. Chem. Soc.,* **77**, 334, (1955).